Optical impedance matching studied with Scanning Near-Field Optical Microscopy

A thesis submitted to the University of Dublin for the degree of Doctor in Philosophy by

Anselm Gademann

Department of Physics

University of Dublin

Trinity College

Dublin 2

Ireland

December 2002

Declaration

This thesis is submitted by the undersigned to the University of Dublin for examination for the degree of Doctor in Philosophy.

This thesis has not been submitted as an exercise for a degree to any other university.

With the exception of the assistance noted in the acknowledgements, this thesis is entirely my own work.

I agree that the Library of the University of Dublin may lend or copy this thesis upon request.

Anselm Gademann

December 2002

Dublin

Summary

This thesis is a study of reflection-mode Scanning Near-Field Optical Microscopy (SNOM). A microscope was built for non-invasive imaging of samples, with optical resolutions better than the diffraction limit. The microscope also incorporates a mechanism for imaging the topography of a sample with a resolution better than 30 nm. The newly implemented shear-force system is based on a tuning fork method and therefore does not rely on an additional laser close to the tip apex. The design of the SNOM and of a fibre pulling machine for producing optical fibre tips will be presented, along with results obtained on test, calibration and transmission line samples.

The heart of the microscope is a tapered and metal-coated optical fibre tip. This is produced by fibre pulling or chemical etching. Metal is evaporated to form an aperture < 150 nm at the tip. Laser light is coupled into the untapered end to create a "light source" with the dimension of the aperture size.

The thesis includes discussion on artifacts encountered in the reflection mode SNOM. Optical resolution down to 60 nm were observed.

The prime focus was to investigate polarisation effects in reflection-mode SNOM. The structures investigated were coplanar transmission line type structures. Two types of transmission line samples were designed and were manufactured by e-beam lithography. The structures consisted of arrays of metal lines (Au, 1 μm wide) on a dielectric substrate (Si). The first structure had the same gap width (250 nm) between all the lines, representing one impedance value. The second part consisted of lines with varying gap width

(200nm-1000nm) representing different impedance values.

Imaging the samples with TM- and TE-polarisation shows a contrast reversal for both samples, explained as a preference of light to exit the tip depending on the structure and the polarisation. When the light is TE-polarised it is more likely to exit the tip compared to TM-polarised light. When imaging the sample with different impedance values a change in the intensity of the maximum in the gap can be observed when imaging with TE-polarised light. This was in line with approximations based on optical impedance matching. When the impedance values of the fibre tip, modeled as circular waveguides, and the transmission lines, coplanar striplines or waveguides, match a maximum energy transfer occurs. This was also observed by us in the near-field experiments and can therefore be used as a suitable explanation.

Acknowledgements

I would like to thank everyone that helped me over the past four years, either through their advice, help in making samples or tips, encouragement and friendship.

In particular I want to thank my supervisor, Prof. Igor Shvets for giving me the chance to this project and for his encouragement and advice over the duration of the four years. I wish you all possible success for the future of the Nanotechnology Group. I also want to thank Dr. Colm Durkan for the advice and the patience in making transmission line samples for me.

I also want to thank Remy Maurice who was helping me with the HF etching of the optical fibre tips for the last two years in the Microelectronics department.

More specifically I want to thank various members of the Nanotechnology group, including Shane for his friendship and the help he gave me especially during the rough times of my project; William for sharing essential parts of the system and the labs with me, as well as listening to me when I got more narky towards the end; Roman for giving me advice towards the Shear-Force system and looking after the Server when I didn't have the time; Guido for listening to all my big amount of complaints about everything at the end and going out for lunch to all sorts of Indian restaurants; Dmitri for being a great house-mate and dragging me off for coffee; Sergei for helping me with some of the mathematical problems I had at the beginning; Jürgen, Ciarán, Luca, Diarmaid, Vivienne, Sergio, Victor, Giuseppe, Ken, Alex and all the new postdocs and postgrads.

I also want to thank the French summer-students, Frederic and Laurent (William of course as well), for testing the pulling machine and pulling fibres and capillaries to test its functionality.

I should also thank the NanoSNOM network participants in giving great advice during the meetings. They encouraged me to continue on to the end, especially Stephanie for providing a couple of tips at the beginning when we had a lot of trouble producing them on our own; Dr. Dieter Pohl, Prof. Othmar Marti and Dr Joachim Krenn for their advice.

As for the technicians I want to thank Tom Burke and John Kelly for organising most of my orders and keeping up with me pestering them all the time. Marie for organising all different sort of things during the end. Dave and Mick for machining some of the components for me or giving me some advice how to do it.

I owe a great deal to my parents and my grandfather. They were always encouraging me to continue when I was down. Their encouragement made it possible for me to finish this project, even when I had doubts during the four years.

Finally I want to thank Looi for constant encouragement and putting up with me for that long, even when I was in a constant bad mood while writing up. I hope that I can give some of this back at a later stage.

Contents

List of Figures

List of Tables

Chapter 1

Introduction to Scanning Near-Field Optical Microscopy

This chapter gives an introduction to Scanning Near-Field Optical Microscopy (SNOM). It will first give a historic overview from the first developments to the actual instrument. This will be done in chronological order starting in the last century with the diffraction limit, the first ideas about a microscope with "super"-resolution and finishing off with the final developments needed to actually build such an instrument. The second part of this chapter will then outline the different available configurations for SNOM. The third part of the chapter will give references to theoretical papers. At the end of this chapter an introduction to impedance matching experiments performed before will be given.

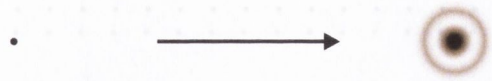

Ideal Point Source

Ideal Point Source as seen
in Microscope due to Diffraction

Figure 1.1: This image shows how a point source would be imaged by a microscope with diffraction.

1.1 Diffraction Limit

At the end of the last century it was clear that there is a limit to the resolution achievable with optical microscopes. This limited the ability of an optical microscope to resolve objects with dimensions $< 250 - 300$ nm, depending on the illumination wavelength. E. Abbe had developed a theory to explain the image formation in the microscope [1], which showed that the resolution limitation was due to diffraction. The result of his analysis was that two objects separated by a distance d, when observed with incoherent light of wavelength λ and using a lens with numerical aperture NA are not resolved when $d < \frac{0.61 \cdot \lambda}{NA}$. Whether the two objects are resolved or not is defined by the so-called "Rayleigh Criterion" [2,3]. The basis for this is that whenever a point source is imaged using a lens system, the image of the point will have a finite extent due to diffraction. This is demonstrated in figure 1.1.

The Rayleigh Criterion states that two of such point sources are just resolved when, in the image plane, the first minimum of one coincides with the principal maximum of the other. This corresponds to a dip in the central intensity of approximately 20%, as shown in Figure 1.2.

As an example we consider a point source which is imaged by a lens with

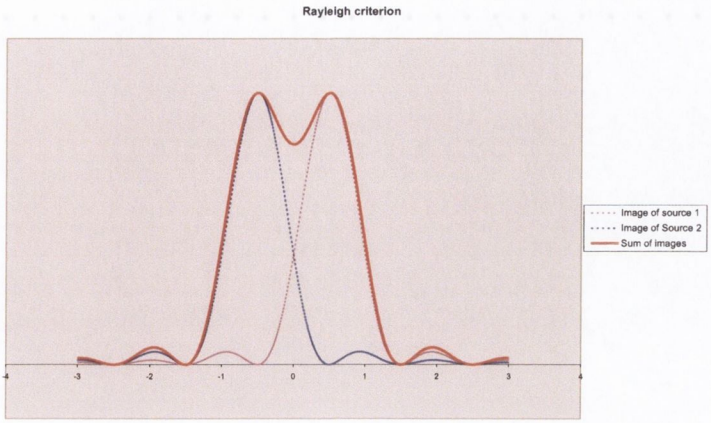

Figure 1.2: The Rayleigh Criterion shows a 20% dip in the central intensity.

an acceptance angle θ of the aperture. Fourier Optics can be used to calculate the intensity distribution of the light through the aperture.

Considering a point source described by the emittance:

$$f(x) = \delta(x - x_0) \tag{1.1}$$

This has a 1-dimensional angular spectrum described by:

$$f(k) = \int_{-\infty}^{+\infty} \delta(x - x_0)\, e^{ikx} dx = e^{ikx_0} \tag{1.2}$$

Observing this point source with a lens of aperture 2θ, only spatial frequencies in the range $\left[0, k_{max} = \frac{\omega}{c \cdot \sin\theta}\right]$ are accepted.

Therefore, the image observed is:

$$f(x) = \int_{-k_{max}}^{+k_{\max}} e^{ikx_0} e^{-ikx} dk = \frac{2\sin\left[\frac{\omega}{c \cdot (x - x_0) \cdot \sin\theta}\right]}{(x - x_0)} \tag{1.3}$$

The width of this spot is:

$$Width = \frac{\lambda}{2 \sin \theta} \tag{1.4}$$

This shows that the "point source" has a finite dimension when imaged with a lens system. This dimension is approximately half the wavelength of the light used. The lens system behaves as a low-pass filter for the spatial frequencies, where the cut-off frequency is $\frac{\omega}{c \cdot \sin \theta}$. This behaviour of the imaging system is the reason why the resolution is limited. This is the conventional diffraction limit. Now the Rayleigh Criterion, as described earlier on, can be used.

At the end of the last century it was thought that this limit is fundamental and could not be circumvented. The problem though is that Kirchhoff's theory, describing the diffraction of electromagnetic waves, is a scalar theory (the same is true for Frauenhofer and Fresnel Diffraction, which are limiting cases of Kirchhoff's theory). This is not sufficient to probe the problem of the diffraction limit deeper, as it is not exact (scalar theory describing the behavior of vectorial fields).

Kirchhoff's theory is inconsistent with Maxwell's theory because it assumes that diffracting obstacles are perfectly black (they absorb all the radiation incident on them, and reflect none). Cases with finite conductivity and dielectric constant of the diffracting obstacles have been studied (Mie 1908 [4]), but these are very complicated.

The first rigorous treatment of a diffraction problem was performed by Sommerfeld [5] in 1896. He looked at the 2-D case of a plane wave diffracted by an infinitely thin, perfectly conducting half-plane, and found the same results as Fresnel and Kirchhoff. Other diffraction problems have been tackled

since then (e.g. Rayleigh [6], Bouwkamp [7]).

Another formulation of the diffraction limit may be arrived at using the Heisenberg uncertainty principle [8–10]. Considering the electromagnetic field distribution at a point $P(x, y, z)$ inside an object to be described by fields of propagating constant $k(k_x, k_y, k_z)$, with $k = \frac{2 \cdot n \cdot \pi}{\lambda}$, n being the refractive index of the material. If the uncertainty in the position of point P is Δx, Δy, Δz, and the uncertainty in the magnitude of k is Δk_x, Δk_y, Δk_z, then the uncertainty principle states that $\Delta x \geq \frac{1}{(2 \cdot k_x)}$. Therefore Δx can only take small values if k_x is large. To determine the largest value k_x can take, it can be written as

$$k_x = \sqrt{|k|^2 - (k_y)^2 - (k_z)^2} \tag{1.5}$$

If k_y and k_z are both real, then the maximum value k_x can reach is k. In this case the diffraction limit follows. However, if either k_y or k_z can take complex values, k_x can become much larger than k. In such a case Δx can now become very much smaller than $\frac{\lambda}{2}$. This means that there can be significant differences in the field pattern over a very small distance. A general situation is that k_z is complex, where k_x and k_y are real. This may be understood with figure 1.3. Figure 1.3 shows the field emitted by a small radiating charge distribution. It was shown, theoretically [11], that the field emitted or scattered by an object with subwavelength sized features, contains a spectrum with a complex propagating constant, corresponding to spatial frequencies matching those of the features, as well as some with a real propagating constant. The waves with real propagating constants contain information about features of the size $\frac{\lambda}{2}$ and greater, while the waves with complex propagating constants

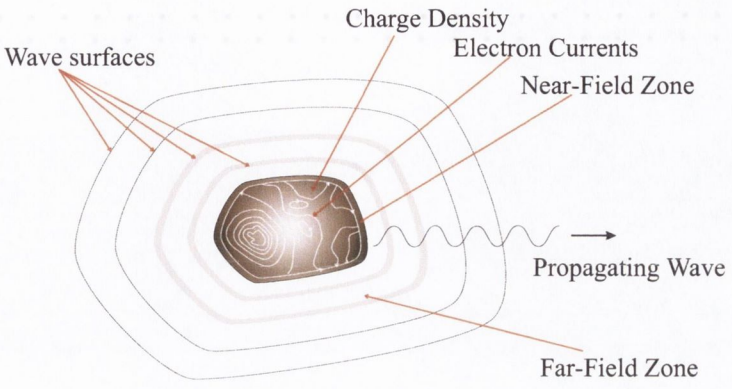

Figure 1.3: This image shows the field distribution of a radiating charge

relate to features smaller than $\frac{\lambda}{2}$. The waves of complex propagation constant are of the form

$$U(x, y, z, t) = A(x, y)\, e^{i\cdot(k_x x + k_y y - \omega t)} e^{(-\alpha z)} \tag{1.6}$$

They decay exponentially away from the surface. The higher the spatial frequency (smaller objects), the greater is the decay (α). These non-propagating waves are also called evanescent waves. They can not be detected in conventional (far field) microscopy. Conventional microscopes can only detect waves with real propagation constant (propagating waves), therefore all information below $\frac{\lambda}{2}$ is lost.

An example of an object scattering light into both propagating and non-propagating components can be seen in figure 1.4. It shows a spherical dielectric particle with radius a, and dielectric constant ϵ. It is irradiated by a plane wave of the form

$$\vec{E}_{in} = \vec{E}_0 \cdot e^{ik\cdot r} \tag{1.7}$$

with the usual time dependence $e^{i\omega t}$.The electric field of the plane wave will induce a time-harmonic electric polarisation in the particle, $\vec{p}$, where $\vec{p} = \vec{E}_{in}\left(\frac{\epsilon-1}{\epsilon+2}\right)a^3$. The electric field at any point is of the form [12]:

$$\vec{E} = \left[3\left(\vec{n}\cdot\vec{p}\right)\vec{n} - \vec{p}\right]\left(\frac{1}{r^3} - \frac{i\cdot k}{r^2}\right)e^{ik\cdot r} + k^2\left[\left(\vec{n}\times\vec{p}\right)\times\vec{n}\right]\frac{e^{ik\cdot r}}{r} \tag{1.8}$$

where $\vec{n}$ is a unit vector pointing in the direction of r, the field point. This equation describes two different regions. The one with $r \gg \frac{\lambda}{2\cdot\pi}$ is dominated by the $\frac{1}{r}$ term, which represents spherical waves travelling away from the particle. This region is the conventional "far-field" region and is characterised by a radiation term.

$$\vec{E}_{ff} = k^2\left[\left(\vec{n}\times\vec{p}\right)\times\vec{n}\right]\cdot\frac{e^{i\cdot k\cdot r}}{r}$$

The other one where $r \ll \frac{\lambda}{2\cdot\pi}$, is also called the "near-field" region. This is dominated by higher order terms, where the largest contribution comes from the $\frac{1}{r^3}$ term. This term is non-radiating, and therefore represents non-propagating waves.

$$\vec{E}_{nf} = \left[3\left(\vec{n}\cdot\vec{p}\right)\vec{n} - \vec{p}\right]\frac{1}{r^3}e^{ik\cdot r}$$

It can also be shown that, for both regions, the time-averaged Poynting vector $\left\langle\vec{S}\right\rangle = \frac{1}{2}\left(\vec{E}\times\vec{H}^*\right)$, where $\vec{H}$ is the magnetic field produced by the oscillating dipole, is zero for the non-propagating waves, therefore they carry no energy from the surface. An estimate of the ratio between the near-field $\vec{E}_{nf}(a)$ and the far-field $\vec{E}_{ff}(a)$ term on the surface of the sphere can be made by considering the field amplitudes squared.

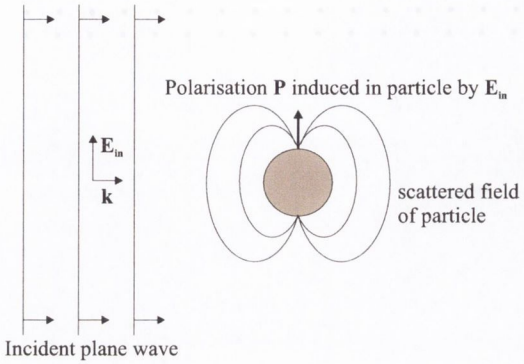

Figure 1.4: Light scattering by small particle

$$\left|\frac{\vec{E}_{nf}(a)}{\vec{E}_{ff}(a)}\right|^2 = \frac{4}{(k \cdot a)^4} \tag{1.9}$$

The consequence is that, for the scattering objects, as the diameter decreases below λ, the near-field terms become more important than the far-field terms. In order to detect these terms, the distance to the detector must be $< \frac{\lambda}{2 \cdot \pi}$. Therefore, assuming that the light source is a Diode Laser with $\lambda = 635$ nm, the detector must be closer than 100 nm to the surface of the scattering object.

The relationship between the scattered and the incident field on the surface is simply

$$\left|\frac{\vec{E}_{nf}(a)}{\vec{E}_{in}(a)}\right| = 2\left(\frac{\epsilon - 1}{\epsilon + 2}\right) \tag{1.10}$$

which, for glass is of the order 0.35. For metals, the surface field is generally enhanced on the surface, and for $\epsilon = -2$, the significant field enhancement corresponds to a surface plasmon [13].

The problem with detecting non-propagating waves is that even when it

is possible to bring a conventional detector close enough to the surface it would not detect the waves. They first have to be "reconverted" into propagating waves. The solution here is that, as mentioned before, every scattering object illuminated by light, produces both propagating and non-propagating waves [11]. Similarly, if this object is brought in contact with non-propagating waves, it will also scatter them into both propagating and non-propagating waves. The propagating part can then be detected. This is the basis for all SNOM techniques.

1.2 Development of SNOM

The first outline of the concept of near-field microscopy was made in 1928 by E. H. Synge [14], who discussed an instrument similar to the modern SNOM. His idea was to place an aperture sized $\sim$ 10 nm at a distance of $\sim$ 10 nm to a sample, which has a surface roughness of $\sim$ 10 nm. He also intended to raster scan this aperture over the surface, in the first article with an arrangement of differential screws and in the second paper [15] by a piezoelectric method. The second method is the one mainly implemented in modern SNOM setups.

In 1944, Bethe published a paper on the theory of diffraction by small holes in an infinitely thin, perfectly conducting sheet [16]. The theory described the electric and the magnetic fields resulting by the diffraction of a plane wave at a small hole (smaller then the wavelength). Bouwkamp showed in 1950 [17,18] that the result was incorrect concerning the near-field part of the calculation, due to a wrong assumption. It was correct for the far-field power term, which was the main point of this paper. Bouwkamp gave an approximate value for the correct field term close to the hole.

Then, in 1956, J. A. O'Keefe independently proposed an ultramicroscope with a similar concept [19]. He pointed out at the end of the article, that the "realisation of this proposal is remote" due to the positioning problems of this aperture so close to the sample.

In 1956, Baez [20] demonstrated that it was possible to image objects (in this case his finger) which were many times smaller than the wavelength of the audio waves used to probe them. This was the strongest indication yet that it was possible to use the Near-Field effect for high resolution imaging.

The first results using electromagnetic waves were obtained in 1972 by Ash and Nichols [21]. They used microwaves with a wavelength $\lambda = 3$ cm, to image a metal grating with a best resolution of $\lambda/60$.

After this no successful attempts were undertaken in the optical regime until the development of Scanning Tunnelling Microscopy (STM) at the beginning of the 1980's [22]. This was due to the positioning and probe production problems.

After the development of the STM two groups Pohl et. al. at IBM Zürich (Rüschlikon) and Lewis et. al. at Cornell University worked on an extension of the Near-Field effect into the optical spectrum.

The IBM group demonstrated the first optical line scan in 1982 [23], showing subwavelength resolution of a step, no specific resolution was claimed. They named the instrument Scanning Near-Field Optical Microscope (SNOM), indicating that it was part of the Scanning Probe Family. Independent of this work, Lewis et. al. at Cornell University were working on a similar technique [24]. They called their system Near-Field Scanning Optical Microscope (NSOM) putting more emphasis on the Near-Field part

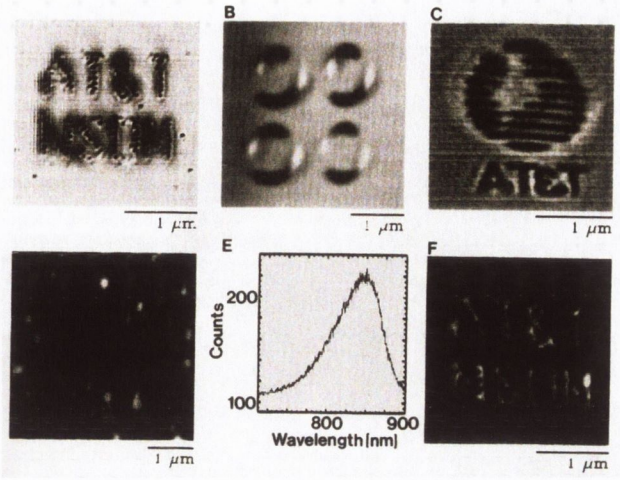

Figure 1.5: Different contrast mechanisms in SNOM. (a) absorption, (b) polarisation, (c) refractive, (d) fluorescence, (e) spectroscopy and (f) reflectivity. Figures shown here are by Betzig et. al. [26, 27]

of the Instrument.

The two main problems these groups had to overcome was the production of suitable probes and the development of a suitable feedback mechanism. The IBM group used Al-coated tapered Quartz rods as probes, while the Cornell group was using tapered micropipettes. The main problem of these probes was the extreme loss of light and therefore the very small output power (10^6 photons/second).

A major breakthrough came with the invention of pulled fibre probes [25]. The throughput of optical fibre probes was $10^4 - 10^6$ times higher than that of the previous probes. The advantage of this was the possibility to implement contrast mechanisms from standard optical microscopy with enough light left to detect the desired effect. Many of them were published by Betzig et al [26, 27] and can be seen in figure 1.5.

The metal of choice to coat the fibres is aluminium due to its small skin depth for optical wavelengths (6 nm). The coating is applied to form a well defined aperture at the end of the fiber tip and to minimise the emission of stray light from the side of the probe. This requires a coating of up to 150 nm and results in an overall diameter of 0.3 μm. The much larger thickness than the skin depth is chosen because of the island growth of aluminium on glass. When the thickness is chosen thinner the coating is prone of pinholes. These pinholes would act as additional apertures and therefore complicating the interpretation of optical images. A thin coating can also result in the excitation of surface plasmons which can then travel to the apex of the tip and scatter there. This would effectively enlarge the aperture to the outside diameter (including coating) of the apex. Using a metal with a skin depth of 10 nm would result in a probe size of 0.5 μm. Due to the rapid divergence of the light from the aperture, the distance to the sample has to be kept constant at the order of 1-30 nm between tip and sample. The tolerance for this is of the order of 1 nm. Therefore, it is impossible to use bigger tips on large surfaces because it is not feasible for such a probe to penetrate the surface features.

The waveguide properties of the fibre tips depend critically on the tip geometry and the coating. The coating is used to produce a well defined aperture. Therefore the disadvantage of a cut-off point is introduced. This is the case as soon as the diameter of the fibre decreases below approximately $\frac{\lambda}{2}$. This can be understood in terms of the field distribution for electromagnetic waves with vacuum wavelength λ_0 travelling through a metallic waveguide of diameter a and refractive index n. The electromagnetic radiation is of the

form:

$$A(x, y, z, t) = A(x, y) \cdot e^{ik_z z} \cdot e^{-i\omega t}$$

where A can be either the electric field, E or the magnetic field, B and where k_z is the propagation constant of the form [28]:

$$k_z = \frac{2\pi}{\lambda_0}\sqrt{1 - \left[\frac{n\lambda_0}{2a}\right]^2}$$

Assuming an ideally conducting metal, k becomes complex once $a < \left[\frac{n\lambda_0}{2}\right]$. Therefore after the tip becomes thinner than the cut-off diameter, the light transmitted through this structure will be strongly attenuated. Most of the light will be retroreflected due to the fact that the structure no longer supports propagating modes. Due to this the transmission of light through the tip may be quite low. The mode which propagates through the metal-coated fibre tip is a HE_{11} mode [29]. This is due to the thin metal coating. An infinite metal surrounding the "tube" would result in a TE_{11} mode.

For increasing taper angle an increase in transmission will be expected. Reported results range from 10^{-6} to 10^{-3} transmission of light coupled into the fibre [25, 30].

Due to the fact that the coating metal is a real metal with a complex refractive index, the propagation constant is always complex.

The coating thickness plays a major role in determining the radiation characteristics of the tip [31]. If the coating is too thin, the evanescent field penetrating into the coating from the inside may generate surface plasmons on the outside of the coating. Because these plasmons experience no cut-off, they may easily propagate to the tip apex, at which point they may radiate.

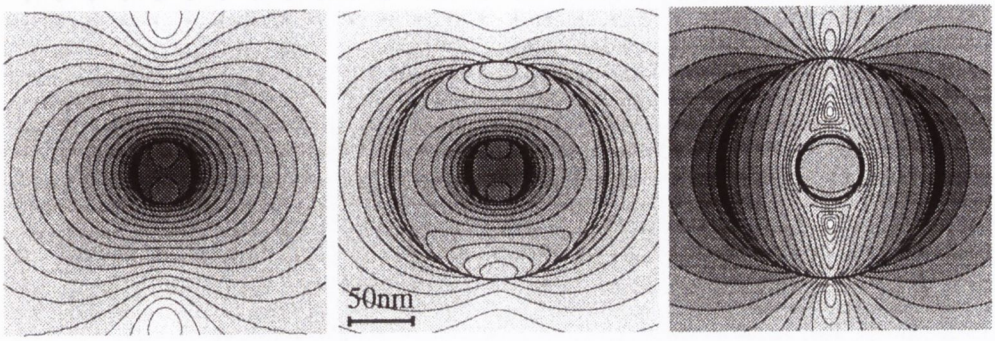

Figure 1.6: Contours of const. $|E|^2$ (factor of $3^{\frac{1}{2}}$ between successive lines) in the aperture planes of three different probes. Left: Infinite cladding. Middle: Finite cladding, field dominated by the flux emitted by the aperture. Right: Finite cladding, field dominated by the flux from the surface of the cladding. [31]

The spot size would then effectively increase to the outer dimension of the tip. Effects of thick and thin coatings are illustrated in figure 1.6.

The best reported resolution with an aperture SNOM utilising coated fibre tips is $\sim 5 - 10$ nm [25], the best for an apertureless geometry is $\sim$ 1 nm [32, 33]. Due to the high dependence of the resolution upon several factors, including topography, polarisation of the light, dielectric structure of the sample and feedback system artifacts, most authors are cautious in claiming high resolution. One example of the type of difficulty that arises is shown in figure 1.7. It shows a topographic image and an optical image of a gold pattern on silicon. The optical image shows a double image. One high resolution image associated with the feedback system and a true optical image with lower resolution. Features seen in both, the topography and the optical image, are marked with blue arrows and represent the high resolution

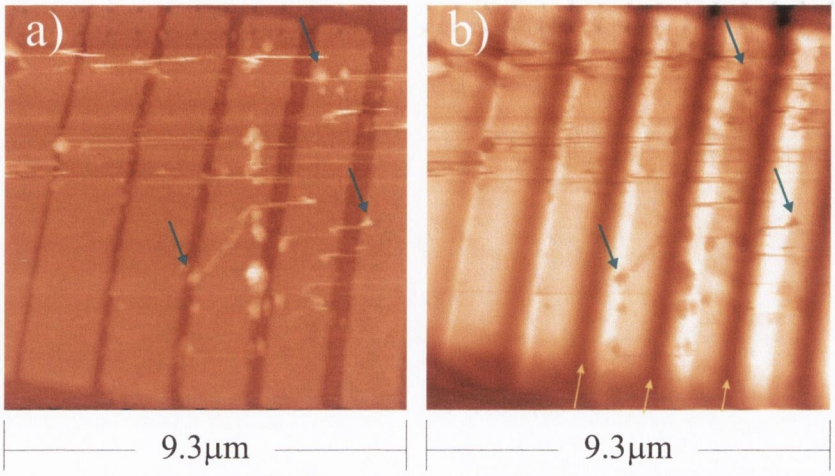

Figure 1.7: Image (a) shows a topographic image of a line structure used in the later experiments. Image (b) shows the optical image of this structure. Two images can be seen, one high resolution one associated with the feedback mechanism and one low resolution true optical image. High resolution features are marked on the topographic and the optical image with cyan arrows. The Low resolution image can be seen in the background and the gaps in between the lines are marked with yellow arrows. A more thorough discussion will be provided in chapter 3.2.

part of the image connected with the topography. In comparison the gaps imaged in the optical image are marked with yellow arrows. For a more thorough explanation please refer to chapter 3.2. This was also observed by Betzig et al [27].

1.2.1 Different SNOM Configurations

Since the initial development of SNOM, several different SNOM configurations have been proposed and developed. A short overview of all of them

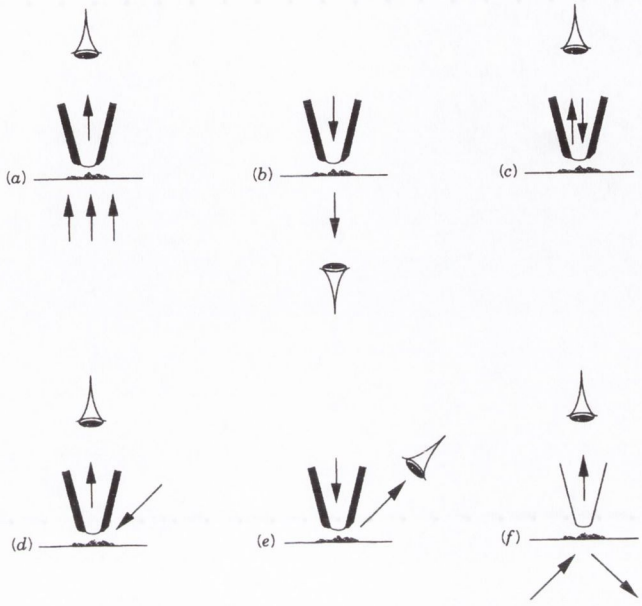

Figure 1.8: Different SNOM configurations available today. Image (a) and (b) show transmission mode SNOM with the tip used for collection or illumination respectively. Images (c), (d) and (e) show reflection mode geometries with the tip being used for collection and illumination (c), for collection (d) and for illumination (e). Image (f) shows the Photon Scanning Tunnelling Microscope (PSTM) [37]

is given here. The following references also have good overviews of different SNOM configurations [34–37]. There are two approaches to SNOM. In the aperture SNOM approach, light is transmitted through a probe with an aperture either for illumination or collection. This approach can be separated into three families with a total of six configurations. The "families" are (1) transmission mode, (2) photon tunnelling mode and (3) reflection mode. The different configurations can be seen in figure 1.8.

The second approach is based on "apertureless" SNOMs [32, 33, 38, 39]. This approach has a very small scattering centre close to the sample to produce evanescent waves or as a scatterer to transform evanescent waves into propagating waves. Some of them are based on existing Atomic Force Microscopes (AFM) [32, 33].

Transmission-mode Aperture SNOM

The first SNOM's developed were based on a transmission-mode geometry. Two different possibilities are available and can be seen in figure 1.8(a,b). They are called collection and illumination mode respectively, depending on the way the tip is used.

One of the first transmission-mode SNOMs, developed by Pohl et al [40, 41], was based on the illumination mode technique, seen in figure 1.8(b). The probes used were quartz rods which were fully coated with aluminium. The aperture was formed by pressing the probe into the sample and monitoring the light output. The tip was then used as a nanosource of light, i.e. in illumination mode. The collection was then performed in the far field on the opposite side of the sample. The feedback system was based on electron tunnelling between the tip and the sample. A sketch of an illumination mode set-up can be seen in figure 1.9

With the introduction of the pulled fiber probe by Betzig et al [25], the tip was not only used as a nanosource but also as a nanocollector. Using it as a nanosource results in the same arrangement as above. The arrangement when it is used as a nanocollector is shown in figure 1.8(a) and is called collection mode. In this case, the illumination comes from the far field and

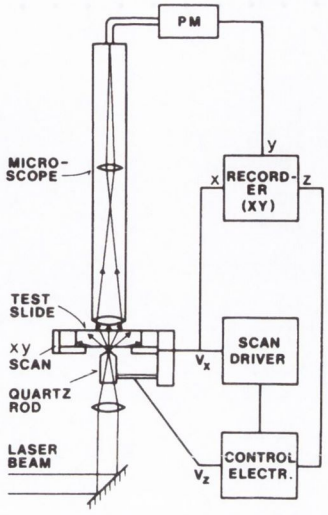

Figure 1.9: This sketch shows the initial transmission mode SNOM used by Pohl et al [40, 41]

the collection occurs in the near-field region. A sketch of a collection type instrument can be seen in figure 1.10.

Initial considerations suggest that both of these modes should yield the same results, but it has been shown that this is not true [43]. This is due to the large area illuminated. It is possible that light from other regions also contributes to the signal collected.

Taking the NFO-7 conference as a benchmark, transmission mode SNOMs account for more than 75% of the presentations and are the most popular commercial systems. They are mainly used in biological and chemical applications. The samples used there are optically thin and therefore allow the transmission of light.

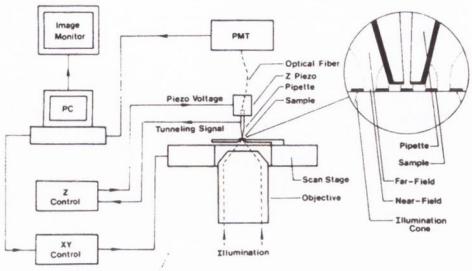

Figure 1.10: This sketch shows a collection mode setup [42]

Reflection-mode Aperture SNOM

One of the most difficult SNOM techniques to realise is the reflection-mode. As many of the samples that would benefit from being studied by SNOM are opaque, the reflection-mode is essential, because transmission mode is not possible for these samples. The first reflection mode experiment was performed by Fischer et al [44] in 1988. A sketch of this initial reflection mode SNOM can be seen in figure 1.11. Since then, more groups have introduced reflection mode experiments, which can be found in references [45–48]. Only a short overview of the different arrangements is given here.

In general, there are three different configurations for reflection-mode SNOMs. They can be seen in figure (1.8 c, d, e); they are illumination / collection, oblique collection and oblique illumination respectively. The difference between them is in the way the fibre probe is used and how the collection and illumination is performed.

In arrangement (c) the tip can be coated [45, 46] or uncoated [47, 48]. It is then used to illuminate the sample and to collect the reflected light. The method with the coated tip is the least promising, due to the fact that there

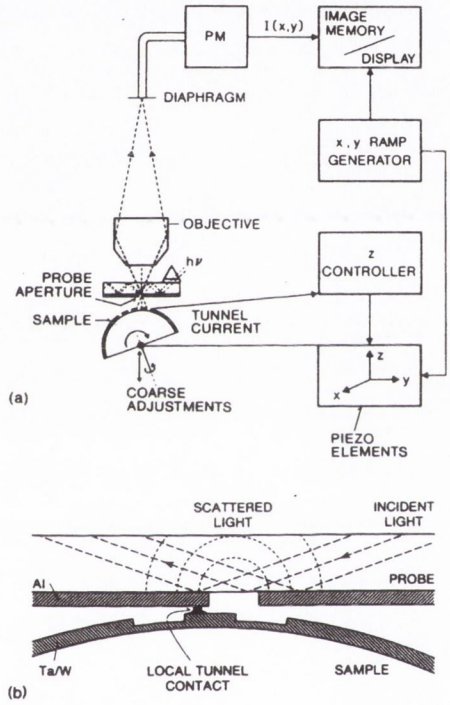

Figure 1.11: This sketch shows the reflection mode set-up used by Fischer et al [44]. The interesting thing to note is that the sample is on a sphere, while the subwavelength hole is on a plate.

is a loss of light transmitted through the aperture in the order of 10^{-6} of the incoming light. Being transmitted twice through this bottleneck would result in a reduction of the light of the order of 10^{-12}, which would mean that the signal is less then 10^{-15} Watts in most cases. The only way to use this is to go for bigger apertures, therefore reducing the loss, and very highly sensitive Photo Multiplier Tubes (PMT).

Arrangement (d) is the collection arrangement where the tip is used as a collector for the reflected light and the illumination is performed from the far field. This can also be used with a self-luminescent sample, e. g. a semiconductor laser. Usually the tip is coated as this improves the resolution.

The third arrangement (e) is the illumination one, using the tip as a micro source and then detecting the signal in the far field [49]. This is the configuration used in this PhD thesis. The actual instrument will be introduced in chapter 2. Tips can be used uncoated or coated, but most groups use coated ones. In our case initial experiments were performed with uncoated tips and later on in the project a switch to coated tips was performed. The uncoated fiber tips were used due to the larger amount of light available to get the first results. In the later stages it was known that the set-up was working and it was necessary to get a better polarisation and better resolution.

Photon Scanning Tunnelling Microscope (PSTM)

One different approach is seen in the Photon Scanning Tunnelling Microscope (PSTM). In this approach total internal reflection is used and the sample is placed above an interface where total internal reflection is achieved, e.g. the flat side of a prism. Above the side with total internal reflection an evanescent

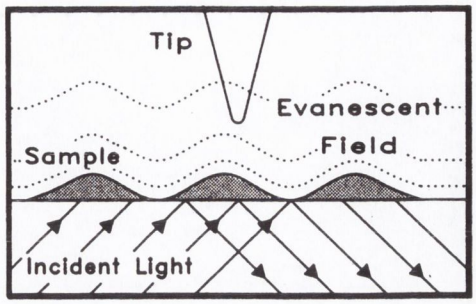

Figure 1.12: This sketch shows the general idea behind a PSTM. An evanescent field is created by total internal reflection at the interface just underneath the sample. These waves are then scattered into propagating light above the sample by a tip and then directed to a collector.

field is created and this is then scattered into propagating waves by a small scattering centre close to the sample which should be studied. The tips used can be metal tips scattering the light to a far field detector. Fibre tips can also be utilised and are usually uncoated, but there is no reason not to use coated ones either, except for the limited light coupling into the fiber through the tip.

The following references give a more detailed description of this type of SNOM [50] and a sketch of the basic principle is seen in figure 1.12.

Apertureless SNOM

Apertureless SNOMs have no aperture as is, which means that they do not use typical tips or other aperture probes. Instead they use either a small particle, metal tips or an AFM tip as a scattering center. This is illuminated with a laser beam when brought into close contact with the sample. The

generated evanescent waves then illuminate the sample. The propagating waves "created" out of the evanescent field are then either detected after transmission through the sample as a transmission type SNOM or in the far field after reflection.

One such SNOM by Silva et al was used for magnetic imaging [38, 39]. The illumination was performed with silver particles, grown on a hemisphere, which were then excited to generate plasmons.

Newer variations of this technique are based on AFM instruments and show extremely good resolution potential [32, 33].

1.2.2 Feedback Mechanism

Radiation emitted from a SNOM aperture remains collimated up to a distance comparable to the aperture radius. After that distance it diverges rapidly. Therefore, to achieve high resolution imaging with SNOM, the tip should be scanned above the sample surface at about 10 nm, with a tolerance of at least 1 nm. Initial feedback methods for controlling this separation included electron tunnelling (STM), due to the possibility to scan at a height of up to one nanometer. The disadvantage of this technique was the limitation to conducting samples. The development of Atomic Force Microscopy (AFM) [51] in 1986 initiated further development into other feedback techniques. This force technique was able to image conducting and non-conducting samples to a scale of a few Angstroms. The AFM itself though was not very well suitable as an aperture SNOM, and there wasn't very much success initially to combine these two techniques.

The development of another "force" technique shortly followed the de-

velopment of AFM, called shear-force [52–54]. The principle is that the fiber tip is oscillated laterally by a few nanometers peak-peak at the mechanical resonance. When this system is brought into close proximity of the sample surface, shearing forces are induced on the tip, which damps its oscillation. This damping can be measured in different ways and then used as a feedback signal. This technique was used as a feedback mechanism during this study, and is very popular with most SNOM groups. It will be described in Chapter 2 and Chapter 3.

The advantage of this type of feedback mechanism is, that it is possible to take a topographic image while measuring the optical one. Therefore the topography-dependent signal in the optical image can be recognised from other signals. All of the images in this thesis were taken this way, except when stated otherwise. The shown topography scans are all globally plane fitted and the optical scans are not processed at all, except when stated otherwise. The Shear-force technique though also has its drawbacks. A closer description of the methods available and used will be given in Chapter 2.

1.3 Theoretical approaches to SNOM

Due to the fact that SNOM is a technique imaging structures much smaller than the wavelength λ used, it is not possible to use conventional ray optics or diffraction theory to model the imaging process. For a full model it is necessary to use a full solution of Maxwell's equations. Only the simplest cases have an analytic solution, for the vast majority of the cases it is necessary to use numerical methods. Due to the low symmetry of most of the SNOM situations, the numerical methods are quite complex. An article by Greffet

et. al. [55] and another one by van Labeke et. al. [56] give an overview on image formation in Near-Field Optics and various theoretical approaches. For the sake of completeness a brief outline of some of them will be given here.

The basic principle in SNOM calculations is to predict the signal detected and therefore the image. To do this it is necessary to solve Maxwell's equation in the tip, in between the tip and the sample, the sample and then the detector. The boundary conditions of the different stages have to be matched. The order of the different parts can vary depending on the type of set-up which is modelled.

A typical SNOM can be considered as consisting of a tip and a sample. The sample is illuminated through the tip, and the near-field distribution coming from the tip is modified and then "detected" via the sample. Alternatively, the sample is illuminated from the far-field and the near-field part above the sample is "detected" via the tip. The different theoretical approaches may be classified depending on the fact whether they include the presence of a tip or not. For example, for PSTM, calculations may be done to determine the near-field distribution above the sample. The "image" can be calculated by assuming some model for the tip detection. This is a non-global approach. These types of models for the tip detection are usually based either on considering the tip as some electromagnetic collector or as a scattering centre. In the first case, which can apply for coated tips, the detected signal can be calculated by using Bethe's and Bouwkamp's results for diffraction by small holes (apertures). In the global model the tip has to be included in the model. This is due to the change of the near-field distribution by the

tips presence. In the global approach the tip and the sample form a coupled system which makes it more realistic, it also makes it more complex.

Another division is whether the tip and the sample are modeled as being continuous solids, or sets of discrete scatterers. The theories are known as macroscopic and microscopic respectively. In the macroscopic models the bulk optical constants are used.

Examples for the different models can be found in the following references [57–61].

1.4 Impedance Matching

The results on polarisation studies in chapter 4 are a continuation of a study started by C. Durkan during his PhD studies [62]. One part of his studies concentrated on transmission line type structures. A contrast reversal was observed when imaging the transmission lines with different polarised light. The samples consisted of simple metal strips (in this case Cr) on glass. They were 1 μ m wide and the gap between them was 250 nm. A sketch of this can be seen in figure 1.13. This figure also shows the notation used for two different types of polarisations. When the light is polarised parallel to the transmission lines it is TM (transverse magnetic) and when it is polarised perpendicular to the lines it is TE (transverse electric).

The initial results were taken with three different types of polarisations. With TM, TE and between the two, at approximately 45° to the lines. When imaging the sample with TM polarised light a large contrast between the line and the substrate (gap) could be seen, but the resolution was low. In this case, the line was imaged as bright (high detected signal) and the gap as dark

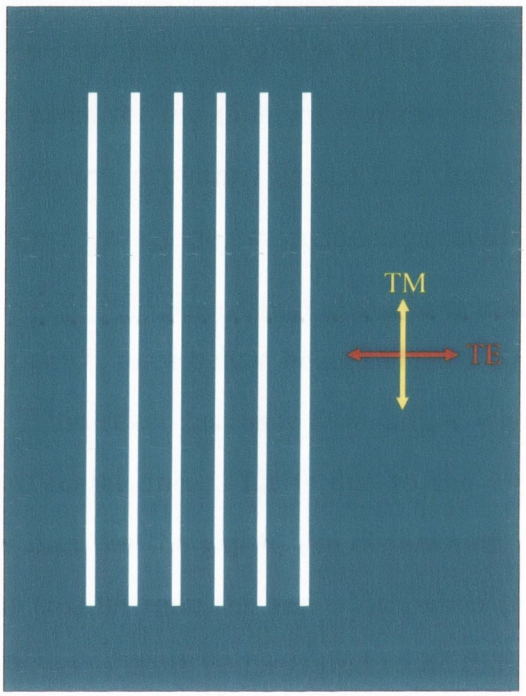

Figure 1.13: A sketch of the sample used by C. Durkan during his polarisation studies on transmission type like structure. It consisted of slotted lines in a Cr-film on glass. The width of the lines is 1 μm and the width of the gap between them is 250 nm. The graph also shows the notation for the polarisation used. TM stands for polarisation parallel to the structures (transmission lines) and TE stands for perpendicular polarisation to the transmission lines.

(low detected signal). When changing the polarisation to a TE polarised light the contrast gets lower and reversed, but the resolution seems to be higher. In this case the line is imaged as "dark" (low detected signal) and the gap is detected as bright (high detected signal). When imaging it with the 45° polarised light it shows the best correlation to the actual object.

The explanation given for the different contrast is as follows. The effect of the TM polarisation was explained by the fact that the light has to pass through an overdamped waveguide (waveguide operated with a larger wavelength than the cut-off wavelength). It not only has to pass through it once in reflection mode, but twice, once before being reflected by the glass and once after the reflection. This effect becomes even larger when the tip is inside the gap between two metal lines. This is due to the metal coating on the tip which effectively narrows the gap to the distance of the tip to the metal lines, which must be smaller than the gap width when the tip is in the gap. Due to this effect, the gaps must be measured to be darker than the lines.

The TE mode on the other hand does not have this type of behaviour. When the light is passing through the gap it does not encounter a cut-off frequency due to its polarisation and the fact that the mode excited in the structures does not have a cut-off frequency. This is when the structures are assumed to be coplanar striplines or coplanar waveguides, which have a quasi-TEM mode as the dominant one. Therefore, the loss through this area is significantly reduced, which can explain the higher intensity in the gap.

This explanation is partly based on microwave theory. The assumption would be to model the tip as a circular waveguide and the printed lines as coplanar striplines or coplanar waveguides. For both of them the en-

ergy loss while coupling energy between the two waveguides is dependent on impedance matching. When a large mismatch exists the loss is high, when they are the same the loss is very low. To verify, whether there is a difference depending on the impedance mismatch has been studied during this study and will be presented in chapter 4.

Chapter 2

Instrumentation

In this chapter, the various elements of instrumentation used and modified for this thesis will be discussed. The first part will describe the reflection-mode Scanning Near-Field Optical Microscope (SNOM) built for the experiments performed during this PhD. This includes a description of the modification of the original setup built by Colm Durkan for his PhD Thesis [62]. The second part shows the methods used to produce fibre probes to be used with the SNOM. The third part describes the feedback system implemented in the SNOM to keep the tip-sample distance at a constant value of around 5-10 nm (within 1 nm) during the scanning. This feedback system is suitable for conducting and non-conducting samples.

2.1 System Design

This section gives a short overview of the mechanical and optical circuits which were built to make the reflection mode SNOM, as well as a brief overview of the vibration isolation system.

2.1.1 Vibration Isolation

The vibration isolation used during these experiments was also used by Colm Durkan during his PhD thesis [62]. Only a brief description of this part of the setup will be given here.

Due to the nature of the instrument involved, which scans with a resolution down to below 50 nm, where the probe is scanned with a distance of just a few nm above the sample [25], a good vibration isolation system has to be used [63]. This reduces the external mechanical vibration to an acceptable level.

The two types of vibrations to which the microscope is subject to are: internal vibration due to scanning movements and external ones. The external ones can come from mechanical vibrations in the surrounding building, as well as acoustic noise. The scanning frequency is in the region of 1 Hz (line frequency) or 200 Hz (dot frequency), therefore the resonance frequency of the setup itself should be as high as possible. Ideally, more than two orders of magnitude higher, so that the setup would not resonate during scanning. However, due to the presence of large moving parts in the system, it is unlikely to have a resonance frequency above 10 kHz.

A sketch of the vibration isolation used can be seen in figure 2.1. The instrument was mounted on a 100 kg optical table, which was placed on four half-filled car tyres that rest on a sand filled frame. This frame was placed on top of a polystyrene damping layer.

Two graphs were recorded using a piezoelectric accelerometer to investigate the influence of the building noise and of a "shock" on the optical table. The first graph (figure 2.2a) shows the noise of the building recorded

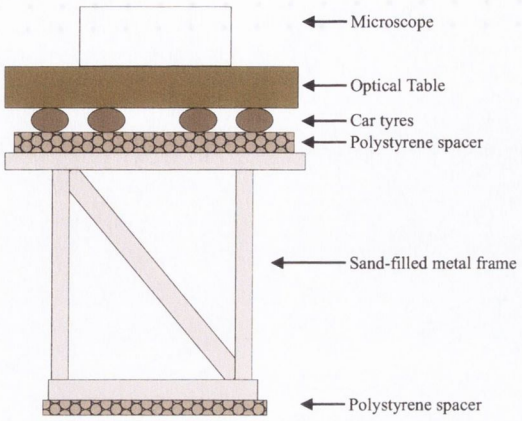

Figure 2.1: This image shows a sketch of the vibration isolation system.

by an accelerometer and displayed with FFT transformation. Two peaks can be seen one at around 9 Hz and the second one at around 90 Hz. The first peak is the same frequency as the resonance frequency determined by the graph 2.2b. The peak at 90 Hz corresponds to construction noise going on in the building. The second graph (figure 2.2b) shows the influence of a "shock", in this case jumping next to the set-up onto the ground. This is the plain recording of the accelerometer and shows the initial shock and the time needed for the damping to finish. The second graph can be used to extract the resonance frequency of the damping system and the Q-factor of it. The resonance frequency is approximately 8.5 Hz and the Q-factor is approximately 10.

Comparing this damping system to commercial ones (e.g. Newport) shows that the resonance frequency is higher (8.5 Hz compared to 1 Hz). But due to the price difference of $>$ \$5000 of the commercial system to the home built system (cost of steel and rubber tyre tubes) we decided to use the home built system.

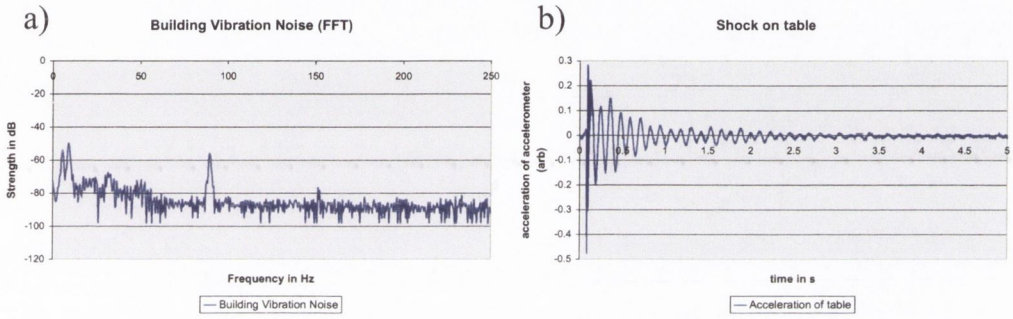

Figure 2.2: Graph (a) shows the noise in the building recorded with a seismic accelerometer. The signal displayed by an oscilloscope using a fast-Fourier transformation (FFT). Two peaks are visible, the first one at around 9 Hz shows the resonance frequency of the damping set-up and one at 90 Hz is due to construction work in the building. Graph (b) shows a shock recorded by an accelerometer when jumping next to the set-up. The resonance frequency of the damping set-up is 8.5 Hz and the Q-factor approximately 10.

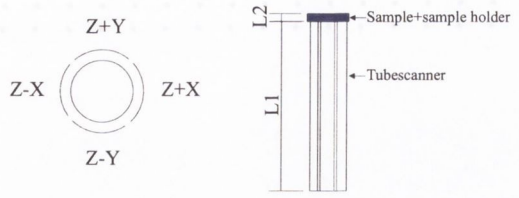

Figure 2.3: This image shows the way the tube scanner is used.

2.1.2 Mechanical circuit for Scanning

Due to the high resolution which is required by a SNOM, it is important to have a stiff design of the actual instrument, and the least number of moving parts. On the other hand, it should also be easy to use. Therefore the majority of the mechanical parts were made from optical components and translation stages (Newport XYZ-translation stages 461-XYZ-M, Newport micrometer screws AJS-0.5, SM-13 and a Newport differential screw DS-4F for coarse positioning [64]). All the other parts were made as solid as possible with as little interfering as possible with the optical light path.

The scanning mechanism was based on a standard piezo-tube scanner with four electrodes on the outside and one electrode inside the piezo-tube. The segments of the piezo tube were used as shown in figure 2.3. This tube had to be calibrated to determine the displacement per unit volt in the X, Y and Z directions. To get an idea of the scan range of the tube the following formulae can be used [65, 66]

$$X = 2 \cdot \frac{\sqrt{2} \cdot d_{31} \cdot L_1^2}{\pi \cdot D \cdot h} \left(1 + 2 \cdot \frac{L_2}{L_1}\right) \tag{2.1}$$

$$Z = \frac{d_{31} \cdot L_1}{h} \tag{2.2}$$

Here, the piezoelectric coefficient $d_{31} = 262 \cdot 10^{-12} \frac{\mathrm{m}}{\mathrm{V}}$, $D = 6.35$ mm $= \frac{1}{4}''$ (mean diameter of tube), $h = 0.5$ mm (thickness of tube wall), $L_1 = 25$ mm, $L_2 \sim 5$ mm.

This gives an expected lateral sensitivity of 32.5 $\frac{\mathrm{nm}}{\mathrm{V}}$ and a vertical sensitivity of 13.1 $\frac{\mathrm{nm}}{\mathrm{V}}$. The Controller used, a WA TOPS2 STM controller, provides a voltage output for X and Y of ± 60 V and for Z of ± 140 V. This corresponds to an expected scan range of 7.80 μm in the horizontal directions (X and Y) and 3.67 μm in the vertical direction (Z).

The calibration was done by using various test samples (line, cross and dot gratings). The results of the calibration will be shown in chapter 3.1.2 for the X and Y calibration and chapter 3.2.1 for the Z calibration. The values calculated had an accuracy of 20% for X and Y and 40% for Z direction. This can be understood by the fact that the piezo tube was not new. This gives the possibility that the piezoelectric material aged over time.

The combined shear-force and SNOM head was machined out of a solid piece of aluminium. It was kept narrow at the front close to the sample to avoid shadowing of the optical signal as much as possible. However, it was made as wide as possible at the end where it is fixed to the translation stage for maximum stability. The holder will be described in more detail at the end of this chapter and in the appendix.

2.1.3 Optical Circuit

The optical circuit employed in our setup is based on a reflection mode geometry. An elliptical mirror (02REM33, Melles Griot [67]) was used to focus the light from the tip/sample combination located at the first focal point

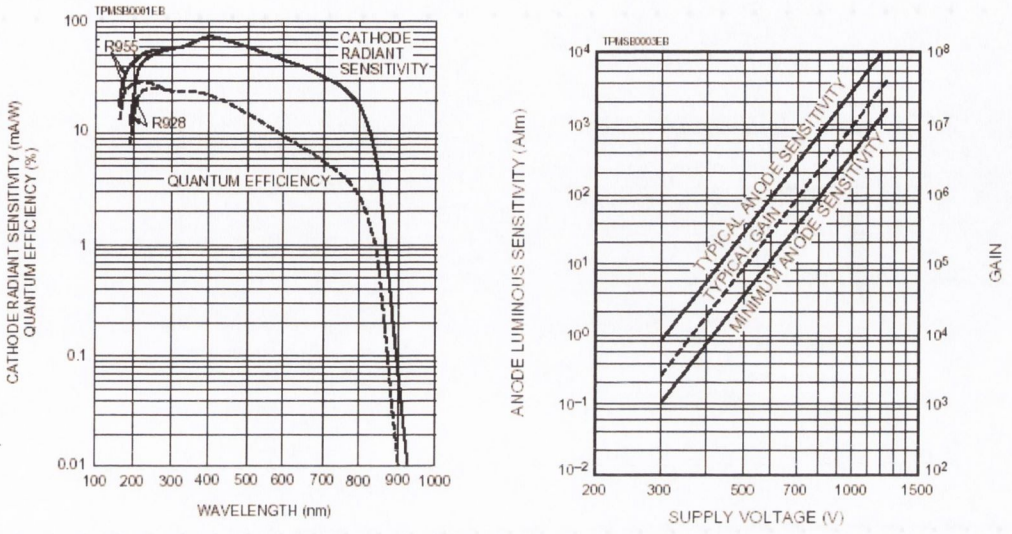

Figure 2.4: This image shows the characteristics of the PMT [69].

into the photo multiplier tube (PMT) placed at the second focal point. The PMT (Hamamatsu model R-928 [68]) used was chosen because of (I) its high sensitivity at the wavelength of the SNOM laser, $\lambda = 635$ nm and (II) the low dark current of 2-50 nA at 1000 V. The gain characteristic of the PMT can be seen in figure 2.4.

For any PMT the current I is proportional to $V^{\alpha n}$ where α is a characteristic of the dynode material and geometry, generally between $0.7 - 0.8$, and n is the number of dynode stages. The PMT in use had 9 stages. Therefore I is proportional to $V^{6.3-7.2}$. It was measured to be 7.4.

As the output signal of a PMT is a current, and most measurement devices (oscilloscope, lock-in amplifiers) have voltage inputs, we had to use an I/V converter. The one used was a Keithley 428 Current Amplifier. For a better signal to noise ratio lock-in detection is used for the optical detection setup (Lock-In Amplifier SRS-830). The laser used in the system is a

diode laser of wavelength $\lambda = 635$ nm and an output power of up to 13 mW (model PMX11/X34, from Laser 2000, U.K. [70]). This laser can be modulated internally from sub-1 Hz to 1 MHz. The resulting modulated output is of a square-wave form with a modulation depth from 0-100 percent. The frequency of modulation we chose is 10 kHz. For higher frequencies the reference photodiode was not "fast" enough to give an accurate frequency reading. Using lower frequencies reduces the possible scanning speed.

The use of an elliptical mirror for the light collection instead of a collection objective has two advantages. The first one is that an objective only collects light from a small region of the whole hemisphere, while the elliptical mirror can collect light from a much larger area. Using a long working distance objective with a numerical aperture of 0.4 gives a solid angle of $\frac{\pi}{16}$, which corresponds to approximately 3% compared to approximately 65% using the elliptical mirror. This can be seen in figure 2.5. The grey area in this sketch corresponds to the approximate area which is collected. The second advantage is that shadowing effects depending on topography are limited. When the light is only collected from one direction shadowing by topographic steps is enhanced. This can be seen in figure 2.6. In this image shadowing will take place if the collection objective 1 is used. In contrast, a maximum will be detected if collection objective 2 is used. With a more symmetric collection of the light (like an elliptical mirror) compared to this directional one (by only using a collection objective from one direction) this "shadowing" effect can be reduced significantly.

Figure 2.7 shows a schematic of the optical part of the SNOM used for this study. In addition to the parts already described, it also includes the

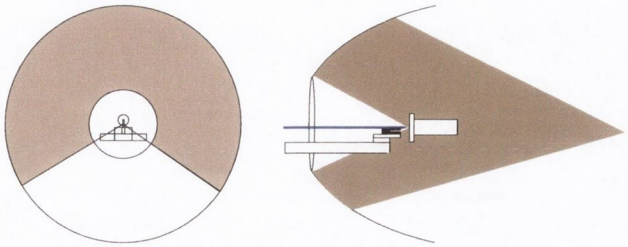

Figure 2.5: This image shows the amount of light collected by the elliptical mirror. The left figure shows the front view of that and the right image a side view.

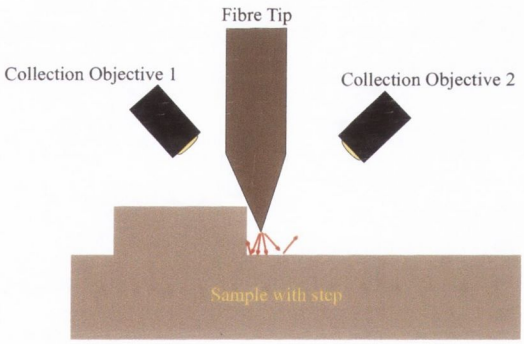

Figure 2.6: This image shows a shadowing effect, when the light is only collected from one side. When the collection objective on the left side is used a minimum will be detected. If the objective on the right side is used a higher intensity will be detected.

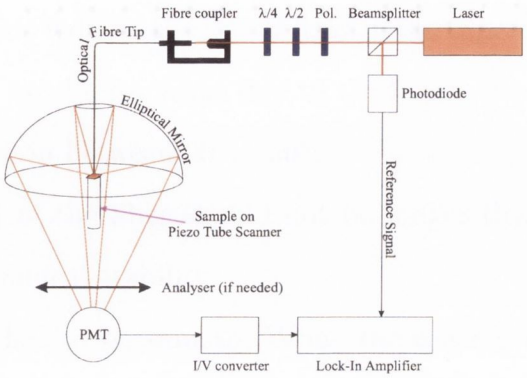

Figure 2.7: This figure shows a sketch of the optical circuit of the reflection mode SNOM.

possibility of polarisation control. The laser is prepolarised by a standard sheet polariser. The polarisation direction can then be adjusted by a half- and a quarter-wave plate. How the polarisation is set for the experiment will be discussed later on in the results chapter for the polarisation experiments.

2.2 Fibre Probes

The most important part of the SNOM is the actual probe used. As described above the most commonly found probe in aperture SNOM consists of a tapered single-mode optical fibre that has been coated with Al. The metal coating is used to produce a well-defined aperture at the end of the fibre, enhancing the resolution of the instrument. This is due to the reduction of the stray light emitted through the tapered part of the optical fibre probe.

The wave-guiding characteristics of the fibre probes are critically dependent on the tip geometry. The criteria to be satisfied are:

1. Large cone angle to shorten the distance between the cut-off point and

the tip aperture. This reduces the loss of light in the tapered region. However, the cone angle can not be too large due to the larger effective aperture [31]. Values should range in between $20° - 50°$.

2. The free end of the fiber should not be longer than a few millimeter ($\sim$ 1 mm) for mechanical stability.

3. The coating has to be smooth. When the coating is not smooth, but grainy, it can enhance the loss of light and gives rise to pinholes and interference and therefore a more complicated image interpretation.

4. The coating has to be thick enough to prevent the rise of surface plasmons, which can then travel to the tip apex and scatter there, effectively increasing the size of the aperture [31]. It should be larger than 30 nm.

To produce the tapered region of the tip there are two general methods. One is a heating and pulling method [25,71,72] and the other involves several etching techniques [73–75], usually with HF. During this study both methods were used and are described below. While heating and pulling was the preferred method with SNOM groups at the beginning, this has now changed and etching seems to be the preferred method used.

2.2.1 Pulled Fiber Probes

The first technique used to produce optical fibre tips was a home built computer controlled pulling machine.

The principle of the heating and pulling process is very simple. The optical fibre is first heated up until it is soft. It is then rapidly pulled apart to thin the fibre down until it breaks to form a tip. In our case the heating was performed by a 20 W CO_2 laser. The laser light is absorbed by the glass and

heats it up to the melting point in around 10 ms. The fibre is clamped to two spring loaded wheels, which are connected to a motor via thin metal wires. When the motor makes a rotation movement the two clamps move apart and a tip is formed. A sketch of the mechanics of this machine can be seen in figure 2.8. The whole process is computer controlled. It is possible to change certain parameters of the process, the most important being the laser pulse time and the time of the delay in between the start of the laser pulse and the start of the pull.

The main problems of this pulling machine were the inaccuracy of the duration in the laser pulse and the small amount of counts needed for the full pulling process to take place. To improve this we applied the following modifications.

The problem with the inaccurate duration of the laser pulse could be easily rectified, by changing the computer controller for a newer computer model. This improved the accuracy of the laser pulse duration to $\pm 2\%$

The second disadvantage of this pulling machine was the small amount of counts needed for the stepper motor to finish the pulling process. To change this there were two options. The first one was to introduce a reducing gear-box in between the motor and the pulling stage. The second option was to go to a different type of pulling mechanism.

The decision taken was to try the second option. A sketch of the new pulling mechanism can be seen in figure 2.9. The "pulling" mechanism is driven by two screws fixed together and to the motor. One of the screws is left-hand orientated and the other one right-hand orientated. A spring loaded nut is fixed on each of these screws and they move away from each other or

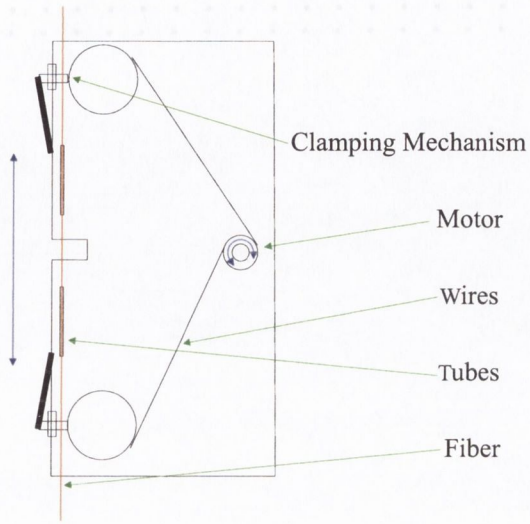

Figure 2.8: This figure shows a sketch of the old pulling machine used in our lab. By rotating the motor the wheels were rotated in opposite directions and the fibre was therefore pulled apart.

together depending on which direction the motor rotates. Two high precision slides are fixed to these nuts via a metal plate where it is possible to fix the fibre. By this change it was possible to increase the counts needed for one full pulling process by a factor of 10.

The new design had to be tested and suitable parameters had to be found. During the initial testing procedure a few thousand "short" tips (fibre $\sim$ 5 cm long) were produced to identify parameters necessary to produce sharp fibre probes. During this testing phase it was shown that due to these changes it was possible to produce probes with an apex diameter of $>$ 200 nm in a reproducible fashion. A yield of better than 80% can be achieved. These probes were useful for initial shear-force results, where the aim was to identify the operation point and for basic shear-force results.

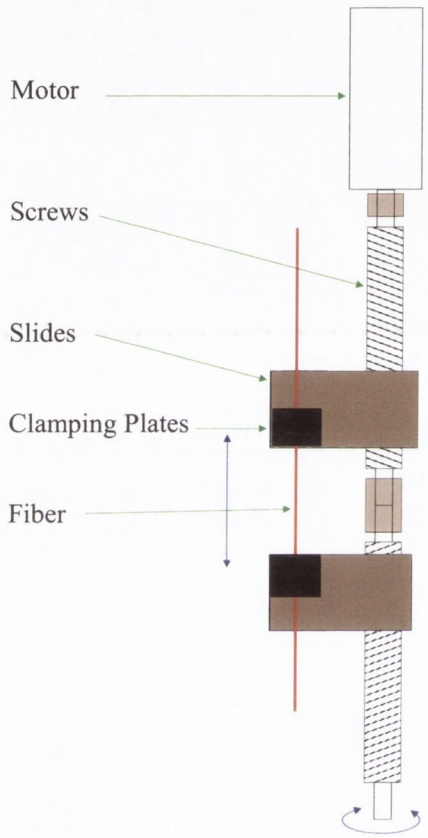

Figure 2.9: This figure shows the pulling mechanics of the new design. It is based on two screws, one left- and one right-hand orientated. When the motor rotates the slides either come together or move apart. The fibre is clamped on the slides by small metal plates.

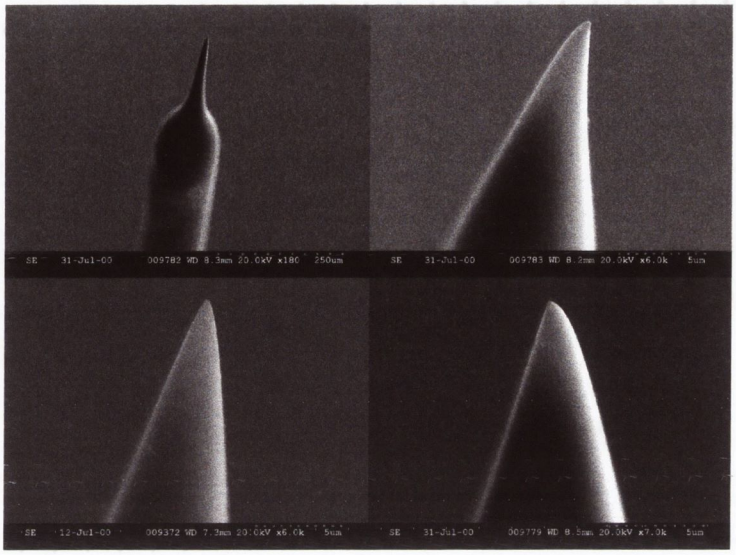

Figure 2.10: These images show some pulled fibre probes.

Probes with a smaller diameter apex were still very difficult to produce and the parameters were influenced by the environment (temperature, humidity ...). When the parameters were optimised on the day, it was possible to produce fibre probes with a yield of up to 50%. Some examples of different fibre tips produced with this machine can be seen in figure 2.10.

Due to this remaining problem with the environmental effect on the pulling process, we also investigated the possibility of etching optical fibre tips.

2.2.2 Etched Fiber Probes

The second method investigated for fibre tip production is chemical etching. There are different etching techniques in use to produce optical fibre tips. Most of these techniques are based on chemical etching in HF solution [73–

75]. The majority of these etching techniques remove the jacket of the fibre before starting the etching process, so that only the cladding and the core are introduced into the etchant. Some of these techniques work by using a two layer etching process, where the tip is formed at the interface of the two layers.

The etching process used in our experiments was based on a technique by Stockle et al [73]. It is the so called tube etching method. In comparison to the other techniques this one does not remove the jacket before etching. The jacket is only removed when the tip is already formed inside.

The steps involved in this etching process are as follows. First the fibre is cut to the desired length and one end is submerged in HF solution. A tip is then formed inside the jacket as shown in figure 2.11. The tip forming process is a convection of the HF inside the jacket of the optical fibre. This convection then forms the tapered region. The time taken for this process depends on the strength of the HF solution. In our case, 34% saturated solution was used and the etching process lasted about 5-8 hours. The fibre tips are then removed from the etching solution and washed to remove the rest of the HF.

The concentration of the HF not only influences the etching time but also the cone angle. An indication of the appropriate solution to obtain a suitable cone angle for the fibre we are using, 3M SN-3224, was given by the original paper of Stockle. Three concentrations were tried during initial testing, 28%, 34% and full concentration ($\sim 45-48\%$). The largest cone angle was achieved with the 34% concentration, as recommended.

After the etching process the jacket has to be removed. This is done by placing the tip end of the fibre into acetone or another solvent. The jacket

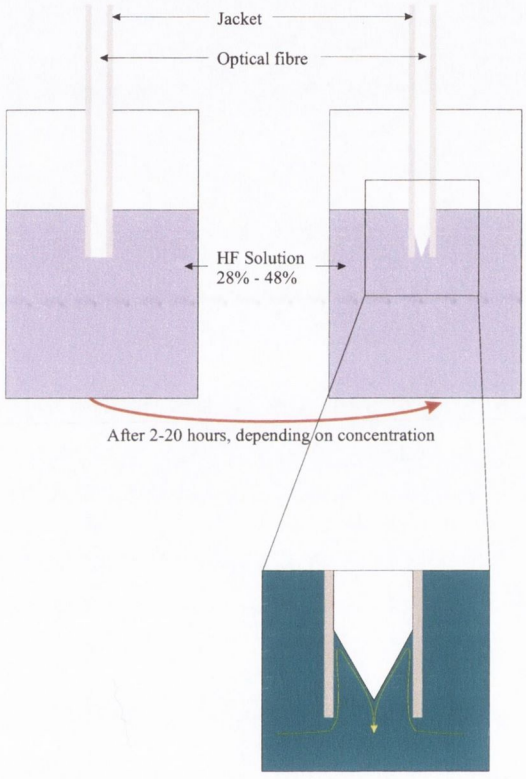

Figure 2.11: This figure shows a schematic of the tube etching process. The fibre is cut to the desired length and then submerged in a 28% - 40% solution of HF. Depending on the concentration a tip will be formed within 22 - 2 hours respectively.

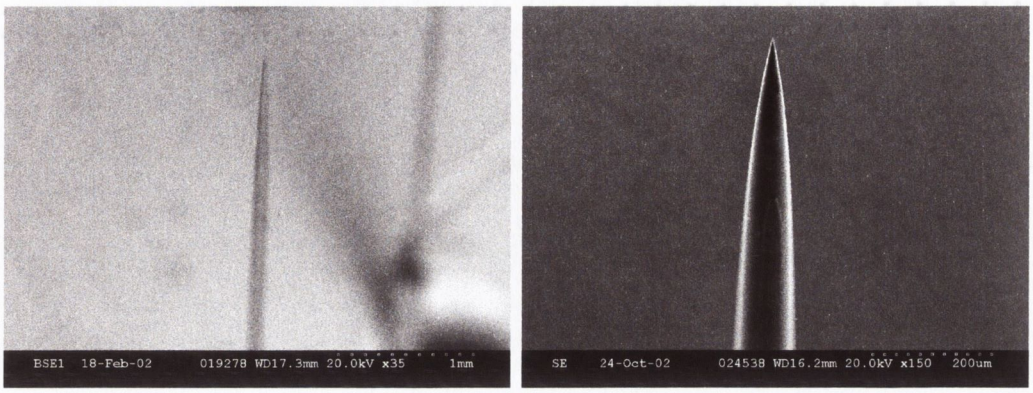

Figure 2.12: This image shows some SEM scans of typically etched fibre probes.

can then be pulled off after a few minutes or it will fall off after a longer period of time. Images of routinely obtained tips can be seen in figure 2.12. The yield of this process is better than 80% when a new etching solution is used.

2.2.3 Coating of Fiber Probes

After the tapering process (pulling or etching) the tip can be used as is, though the resolution is not as good due to stray light from the tapered region. To avoid this, the usual procedure is to apply a metal coating onto the taper and only leaving a small aperture open at the end of the tip apex.

The metal of choice was aluminium. This is due to the small skin depth ($\sim$ 6 nm) at optical frequency [23]. The coating still has to be between 30-150 nm thick to block most of the light out. The coating is applied via vacuum evaporation while rotating the tips above the evaporation source to obtain a uniform metal layer. The set-up used can coat eight tips simultaneously. A

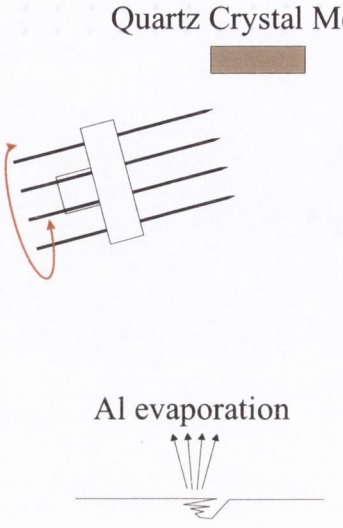

Figure 2.13: This figure shows a sketch of the evaporation set-up. The tips are fixed to a holder (maximum of 8 at a time) and then rotated above the evaporation source. The amount evaporated is measured by a quartz-crystal monitor.

sketch of this setup can be seen in figure 2.13.

The aperture size is controlled by changing the angle θ of the tip with respect to the evaporation source. The angle used in our case is approximately 15°. This was identified by C. Durkan as being the optimum angle of our set-up to achieve an aperture of around 50-150 nm. The DC-motor is mounted on a hinge, so θ can be easily adjusted.

The amount of aluminium evaporated is monitored with a quartz crystal monitor. Due to the rotation of the tips the measured amount only represents the overall thickness deposited on a non rotating surface. This is illustrated in figure 2.14, where the radius of the fibre is r, the overall deposited thickness is d, and the thickness deposited on the rotating tip is t.

Figure 2.14: This figure shows how the metal would be evaporated onto a fibre when it is static or rotating.

The cross-section of aluminium deposited in case one is $2 \cdot r \cdot d$. In the second case, where the fibre is rotated, the amount of material evaporated must remain constant. It is spread over the whole cross-sectional area. The amount of material here is now $\pi (r + t)^2 - \pi r^2$. Therefore we get for t:

$$t = -r + \sqrt{r^2 + \frac{2rd}{\pi}} \tag{2.3}$$

This is plotted in figure 2.15 for a tip diameter of 100 nm and thickness as measured on the quartz crystal monitor from 0-1000 nm and in figure 2.16 for tip diameters ranging from 30 nm - 1 μm with 200 nm measured on the quartz crystal monitor. It is clear that the thickness of aluminium deposited on the tip will decrease towards the tip apex.

The process of producing fibre probes was done due to cost saving measures. The price of one commercial probe is approximately $100. The fact that the probes are very fragile, which can result in short lifetimes justifies the large amount of time invested in producing probes. The probes used in general had a coating thickness of approximately 40 nm, using the values of the thickness monitor. The geometry of the probes were initially verified by

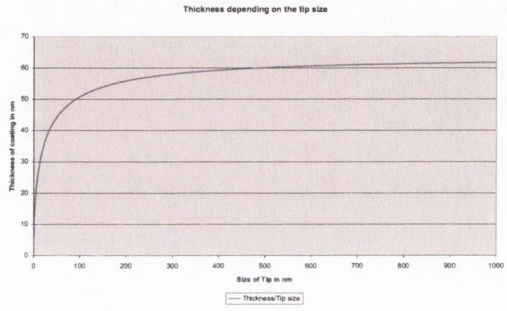

Figure 2.15: This graph shows the amount of metal deposited onto the fibre tip depending on the tip size.

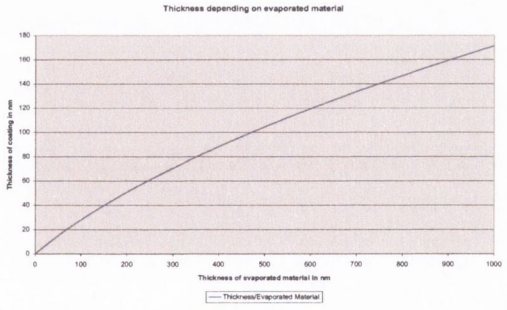

Figure 2.16: This graph shows the amount of metal deposited depending on the amount of metal evaporated.

means of SEM and at a later stage with an optical microscope due to the larger amount of experience.

2.3 Feedback System

As mentioned before in the introduction, the light emitted from a SNOM fibre tip only remains collimated out to a distance comparable to the radius of the aperture of the tip apex [26]. At larger distances the emitted light diverges rapidly. For this reason it is important to keep the probe close to the surface, with a maximum separation of a few tens of nm from the surface.

Before the advent of force microscopy one standard way to achieve this was to use STM as a feedback system to keep the tip at a constant height. This had the disadvantage that the samples had to be conducting. The two force techniques, atomic force microscopy (AFM) and shear-force microscopy [53,54], don't have this problem and can be used to work with non conducting samples.

The technique of choice of a lot of SNOM groups is the Shear-Force technique. This technique involves vibrating a tip horizontally above a sample and then detecting the tip damping when approaching the surface. This is especially convenient when optical fibre probes are utilised, because of their stiffness in the perpendicular direction which makes them nearly unusable for AFM.

To measure the tip damping there are different techniques. One group of techniques is based on an optical approach [53, 76–78] while the other one is based on piezoelectric material [79–82]. The first SNOM in the group incorporated an optical system [76,77], but due to the additional introduction

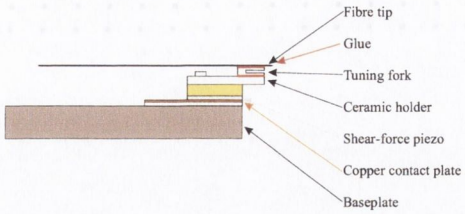

Figure 2.17: Sketch of the Shear-Force mechanism used. It is based on a tuning-fork technique. A thickness-mode piezo is used for exciting the tuning fork. One arm of the tuning fork is glued on the base and the optical fibre tip is attached to the other arm. When the tip approaches the sample a damping signal can be detected using a Lock-in amplifier.

of laser light close to the sample this can interfere with the measurement of the real optical signal. This is especially true when using a reflection mode geometry.

Therefore we decided to change the shear-force system according to the method proposed by Kantor et al [82], which is based on a piezoelectric detection method.

This system is very closely related to the tuning-fork method proposed by Karrai et al [79]. This original method utilised a standard quartz-tuning-fork as a detector of the damping. It was excited by a standard piezo material at its resonance. The tip was glued on one of the tuning-fork arms, while the other arm was allowed to remain free. The Q factor for such a system was above 300. This gave it very good sensitivity, but the drawback was a slow scanning speed due to long damping times.

The difference of the method implemented in our system is that one of the arms of the tuning-fork is attached to the base plate (see figure 2.17).

In comparison to the two free arms used by Karrai the Q-factor is reduced quite significantly to a typical value of 100. This then gives the possibility for shorter time constants and therefore faster scanning speeds. The disadvantage is the lower sensitivity, but during the testing phase this didn't play any major role.

The shear-force system was excited at the resonance frequency by a piezo (in our case a thickness-mode piezo), which was attached underneath the tuning fork. This was excited using a lock-in amplifier (Stanford Research SR850). The signal is then measured at the two contacts of the tuning fork and depends on the amplitude of the fork, which is directly related to the movement of the fibre tip. When the tip approaches close to the sample the movement of it is damped and therefore the measured signal of the tuning fork is reduced. The lower the signal measured at the fork the closer is the tip to the sample. Due to the fact that the controller used for scanning is a standard STM Controller by WA, WA TOPS2, the signal which had to be generated had to mimic the approach curve of a STM tip approaching a sample, so that it would be usable as a feedback signal.

To "emulate" an STM current the signal was offset by the amount measured when the tip was out of contact. This offset made sure that the signal out of contact is 0 and when getting in contact the signal decreases to a negative value. This is the exact same behaviour as an STM signal with a pre amplifier. For more Shear-Force related results please check chapter 3.1.

At the end of this chapter we want to give one more schematic of the full SNOM/SF-set-up in use. This can be seen in figure 2.18. The beamsplitter in the path of the laser beam is used to generate one reference signal with a

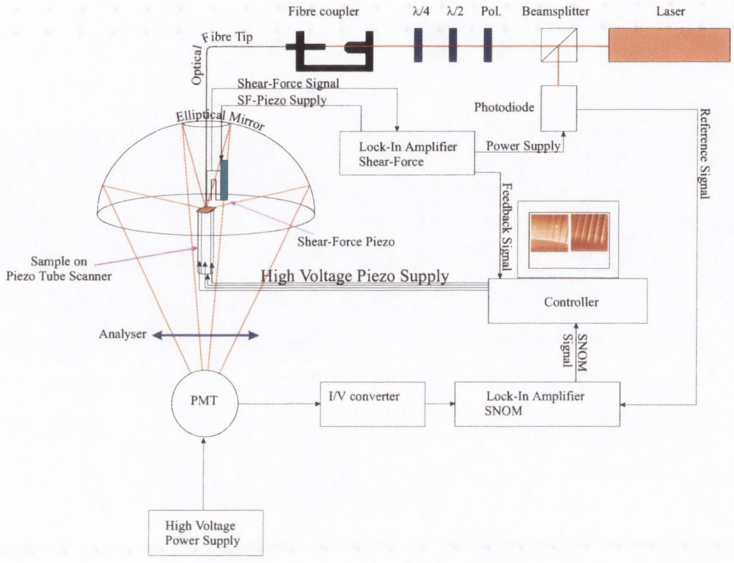

Figure 2.18: Sketch of the whole reflection mode SNOM set-up, with both the mechanical and optical parts.

photodiode, as well as coupling light into the fibre for driving the SNOM.

Chapter 3

Shear-Force and SNOM Results

The first part of this chapter concentrates on the initial tests of the new implemented Shear-Force system and the calibration of the tube scanner. The second part concentrates on the initial SNOM results achieved with the Set-up. The meaning of "in contact" or "contact" from now is that the fibre tip is detecting a shear-force damping signal, it does not mean physical contact, except stated otherwise.

The scan frequency for the scans presented is approximately $\frac{1}{4}$ Hz line-frequency and in between 50-150 Hz dot frequency.

3.1 Shear-Force Results and Calibration

After the implementation of the new shear-force feedback system the performance had to be verified. It was originally developed for fast shear-force scanning on a larger scale [82, 83], up to the millimeter scale. It had to be shown that the system could also resolve nanometer size features.

To check basic shear-force behaviour frequency curves and distance curves

with varying excitation amplitudes were recorded. The system was then tested by using microchip samples to check basic functionality and grating samples to establish the calibration in X and Y for the piezo-tube scanner.

3.1.1 Testing the Shear-Force system

First we tried to detect the frequency with the biggest change between out-of-contact and in-contact situations. This was done by taking frequency/signal curves out-of-contact and in-contact. Afterwards we used this frequency to take distance/signal curves. This allowed to establish the optimal frequency of shear-force operation.

Frequency / Signal curves

Our initial understanding was that the tip when getting into contact would react like a standard harmonic oscillator. This would only result in a damping on the signal. To verify this we recorded frequency / signal curves out of contact and in contact using the internal frequency sweep feature of the Lock-In Amplifier (SR-850), see figure 3.1. The recorded curve out of contact showed a resonance frequency at 32800 Hz. When the behaviour of the shear-force system shows the same behaviour as a simple harmonic oscillator the expected curve would result in a damped resonance frequency. The measured curve showed a different behaviour. In addition to the damping it also showed a shift of the resonance frequency to a higher value of 32870 Hz. This result shows that the behaviour of the shear-force system is more complicated than simple damping. The shift to higher frequency can be achieved when the spring constant also varies when approaching the surface.

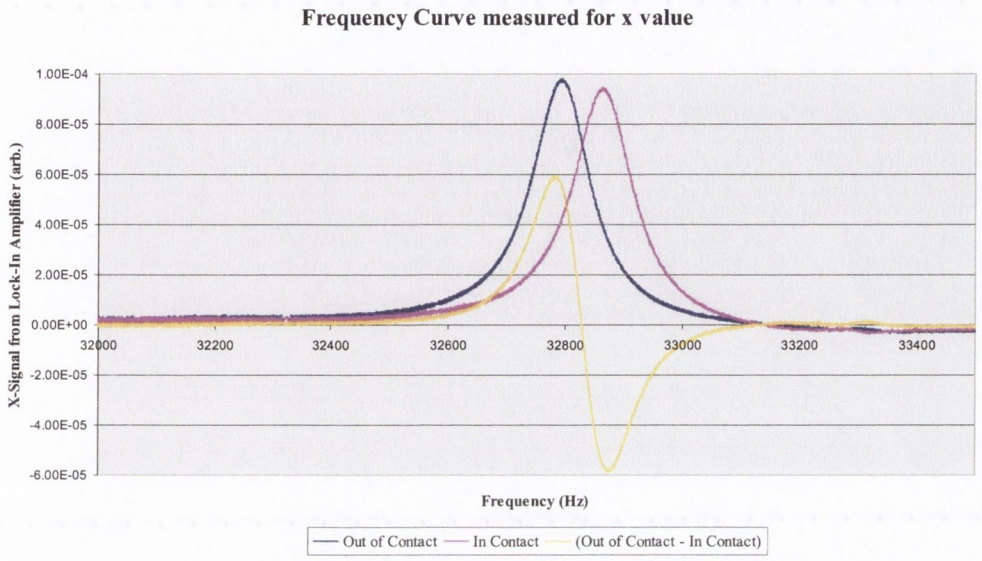

Figure 3.1: Measurement of a frequency curve in and out of contact.

Subtracting the two measured curves "out of contact" and "in contact" from each other shows that the biggest change occurs at a frequency of 32790 Hz. This is just below the resonance frequency of 32800 Hz. Therefore the frequency used for shear-force was just below the resonance frequency "out of contact".

In addition to the resonance frequency the graph (figure 3.1) also gives the Q-factor of the sytsem. In our case the Q-factor was typically around 100 (30-200). The Q-factor gives an indication of the tip movement compared to the excitation amplitude.

$$A_{tip} \sim Q \cdot A_e \tag{3.1}$$

with A_e as the peak-to-peak excitation amplitude, Q the quality factor and A_{tip} the peak to peak amplitude of the tip.

Distance / Signal curves

The next thing to do, was to check how the tip reacts when getting into contact with a sample. This was done to see if the dependence of the excitation strength behaves as expected and to find a suitable operating point for feedback use. Depending on the excitation, the distance of "first"-contact (first time when Shear-Force damping can be registered) to full contact, increases with the excitation amplitude.

The dependencies of the damping on the excitation amplitude were measured by driving the excitation piezo with different voltages from the Lock-In amplifier in use (SR850). The excitation voltages used for this experiment were from 0.2 V to 0.6 V. These voltages result in a thickness change of the piezo of .152 nm to .456 nm and an approximate tip movement of 5 nm to 15 nm.

Depending on the excitation voltage and therefore the amplitude of the tip, the distance of the "first"-contact should change [62]. The larger the amplitude the earlier the first shear-force effect should be seen, and therefore it should be detected further away from the sample. The results for this measurement can be seen in figure 3.2. The shown curves are signal to distance curve and they were performed by moving the tip from out of contact to full contact (touching the sample). It shows the amplitude for three different excitation voltages, 0.2 V, 0.4 V and 0.6 V and it can be seen that depending on the voltage, a significant reduction in the amplitude occurs, as expected. Table 3.1.1 summarises these results. Each value for different excitation values is a mean of 10 or more distance curves and also includes the standard deviation.

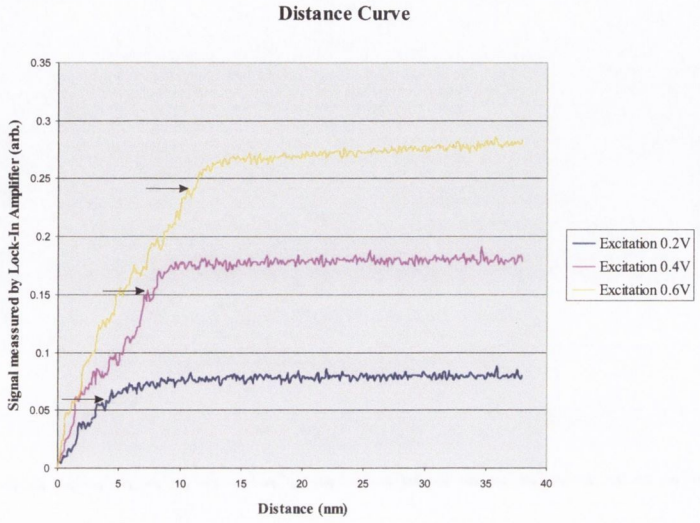

Figure 3.2: Influence of the shear-force excitation on the distance where the first measurable reduction of the amplitude takes place. The curves were measured by moving the tip from out of contact to full contact (test-to-destruction).

Table 3.1: This table gives an overview of the distance of the first Shear-Force contact measured depending on the excitation. This experiment was carried out using a plain glass substrate.

Excitation in V	approx. P-P amplitude of tip in nm	Distance of Shear-Force in nm
0.2	4.6	6.4 ± 1.4
0.4	9.1	9.9 ± 2.2
0.6	13.7	14.0 ± 1.9

The typical operation point for the future use as a feedback system was set at approximately 90% of the signal. This point had enough damping to be detected and was far enough away from the sample to avoid tip-crashes. It also limited the tip wear due to the distance. The operation point is also marked in figure 3.2 with arrows for the different excitations.

Scans of Microchip samples

We have used two different types of commercially available microchip dies (plain microchip die without casing) as functionality samples.

The first sample used was a standard signal processor by Texas Instruments (Venus). It contained various types of features – two of which had the desirable dimensions for the tube scanner (500 nm -4 μm). The first of these features were circuit lines on the processor ($\sim$ 500 nm wide). They were either individual lines or arrays of lines bunched together. An example of each can be seen in figure 3.3 a and b respectively.

Representative shear-force images of the first type of feature are shown in figures 3.4a-d. A cross section across the lines of figures 3.4a and c can be seen in figure 3.4.

The representative scan of the second type of feature can be seen in figure 3.5a. The cross-section is shown in figure 3.5b.

The scans in figures 3.4 and 3.5 show a good correlation when compared to the optical microscope images in figure 3.3

The second microchip sample was a memory chip by NEC (SRAM). This one had very consistent features in the memory area. They consisted of lines that overlapping one another. The lines were approx. 1.3 μm wide. An optical

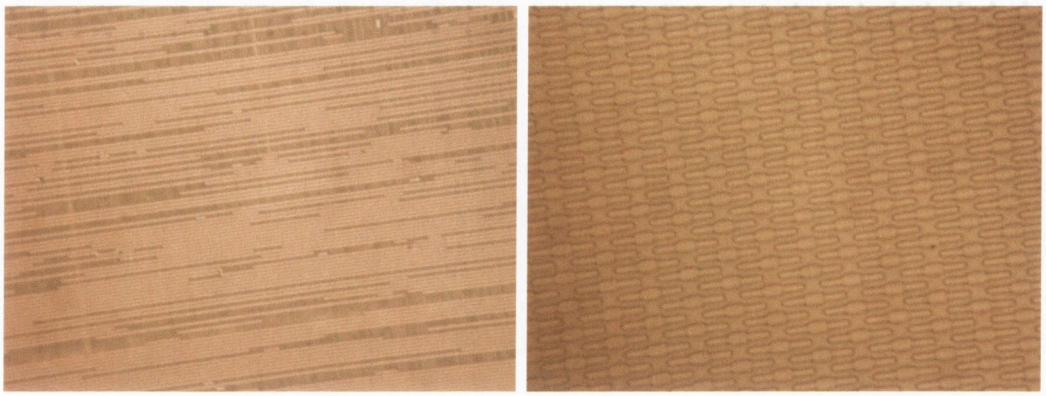

Figure 3.3: This image shows two optical microscope image of the two features on the Venus Microprocessor. The size of the images is approximately 70 μm$\times$ 100 μm.

microscope and a SEM image can be seen in figure 3.6. The SEM scan also shows that the distance in between the different lines is approximately 300 nm. The shear-force scans of one of these areas can be seen in figure 3.7, showing the same shape as expected. The cross-sections indicated in figure 3.7a,b are displayed in figure 3.7c,d. Comparing the sizes of the lines imaged with shear-force to the ones with SEM shows that the gap is smaller and the lines are wider than expected. This is due to tip-induced broadening. This is a limitation of all scanning probe microscopes. The finite size of the tip widens structures higher than the substrate, while it images gaps smaller than they actually are. Another limitation is the wear of the fibre probes. Even when scanning with a non-contact instrument contact will occur over time, especially when a sample with topographic features is imaged. Therefore it is not always possible to use the same tip for very long experiments due to the loss of performance towards the end.

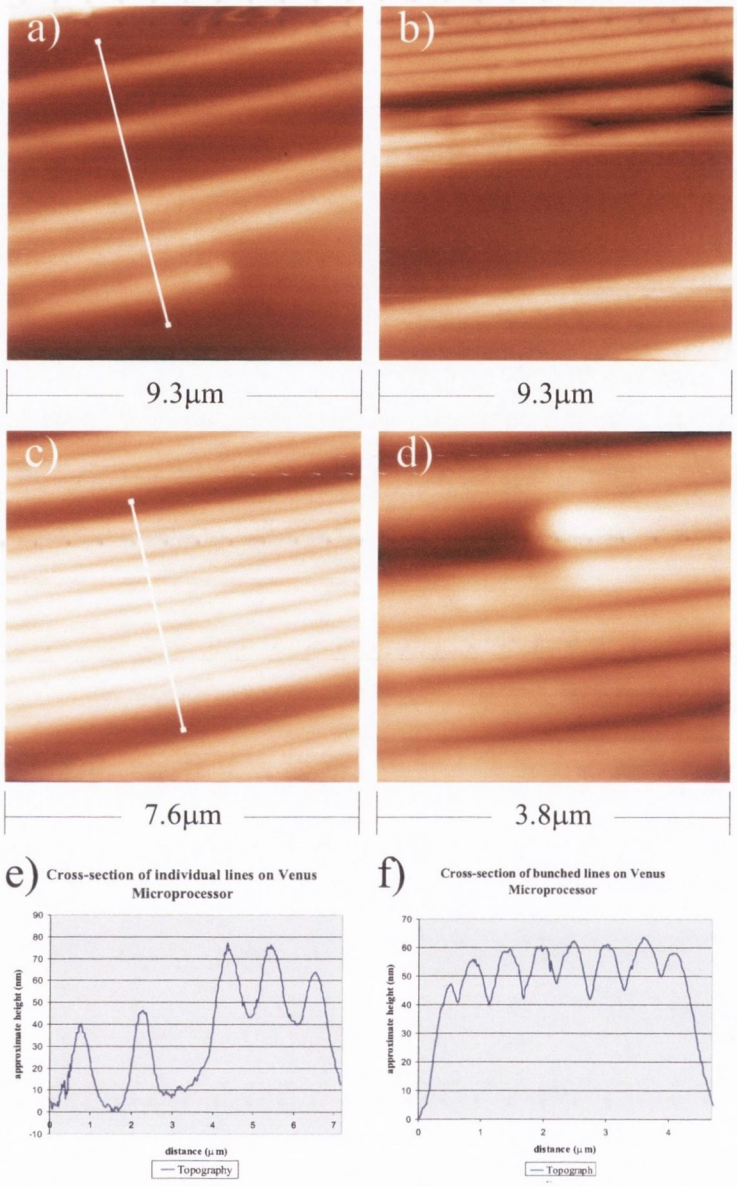

Figure 3.4: Shear-force scans a and b show individual lines of the microchip circuit, while c and d show bunched lines. The scan dimension for a and b approx. $(9.3\ \mu\text{m})^2$, for scan c it is approx. $(7.6\ \mu\text{m})^2$ and for scan d approx. $(3.8\ \mu\text{m})^2$. The line on image a and c indicate the position where the cross-section shown in graphs e and f are taken respectively.

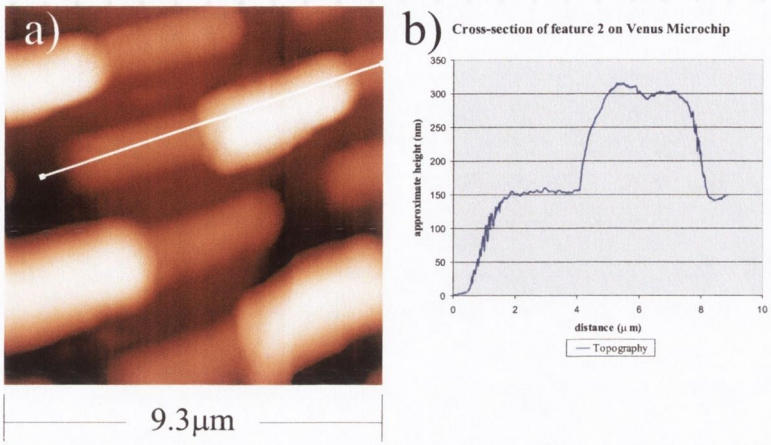

Figure 3.5: The shear-force scan (a) shows a scan of the second feature of the microchip. It can be seen that it consists of a line with an additional feature on top. This is also shown by the cross-section (b). The scan dimension is approx. $(9.3\ \mu\text{m})^2$.

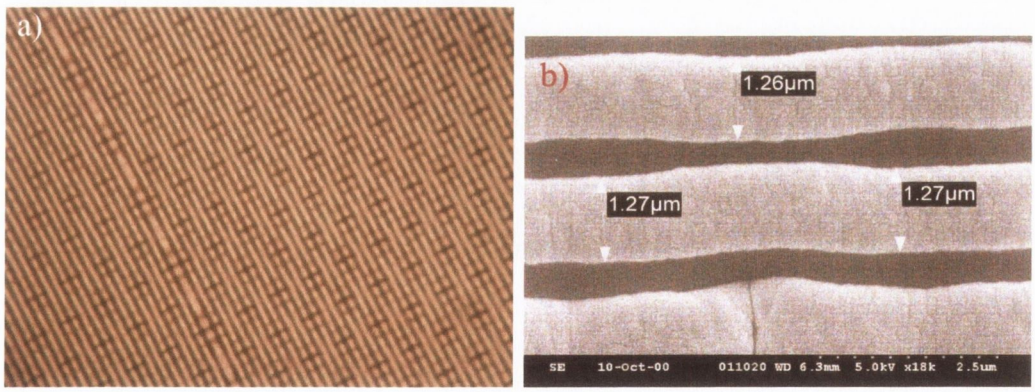

Figure 3.6: Image (a) shows an optical microscope image of the area scanned on the chip die (size approx. $70\ \mu\text{m} \times 100\ \mu\text{m}$). Image (b) shows a SEM scan. The size of the lines is approx. $1.3\ \mu\text{m}$ and the gap in between two lines is 300 nm.

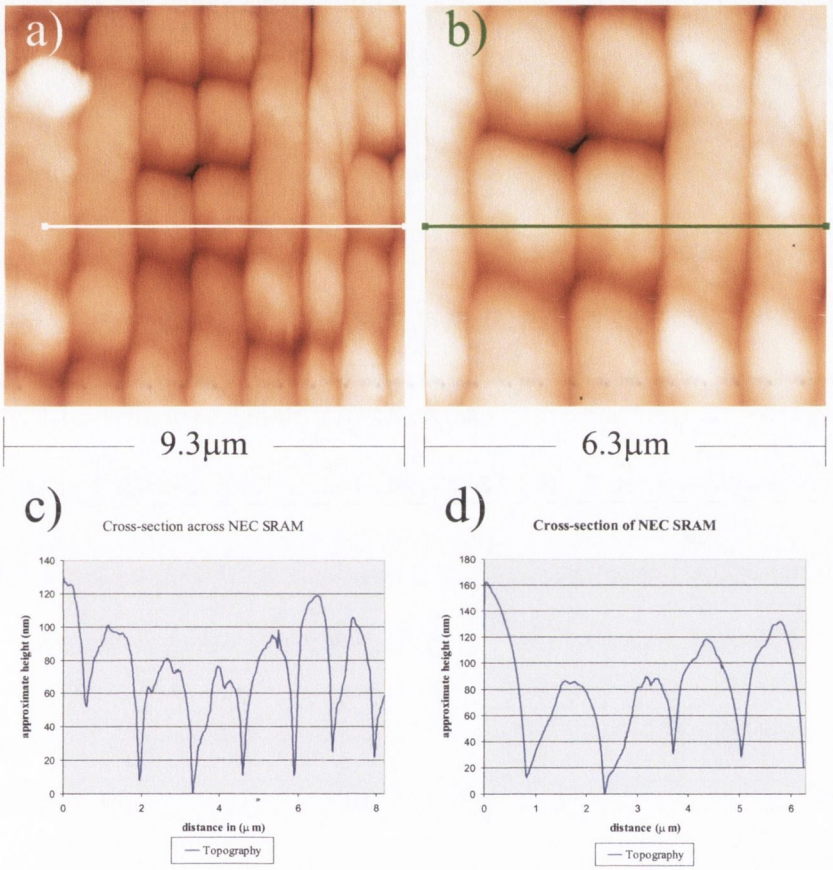

Figure 3.7: These scans show typical shear-force scans achieved on the NEC SRAM sample. Scan (a) has a dimension of $(9.3\ \mu\text{m})^2$ and scan (b) is a zoom in with a dimension of $(6.3\ \mu\text{m})^2$. The lines indicate where the cross-sections shown in graphs (c) and (d) were taken respectively. The cross-section shows tip induced broadening compared to the SEM scan of figure 3.6b.

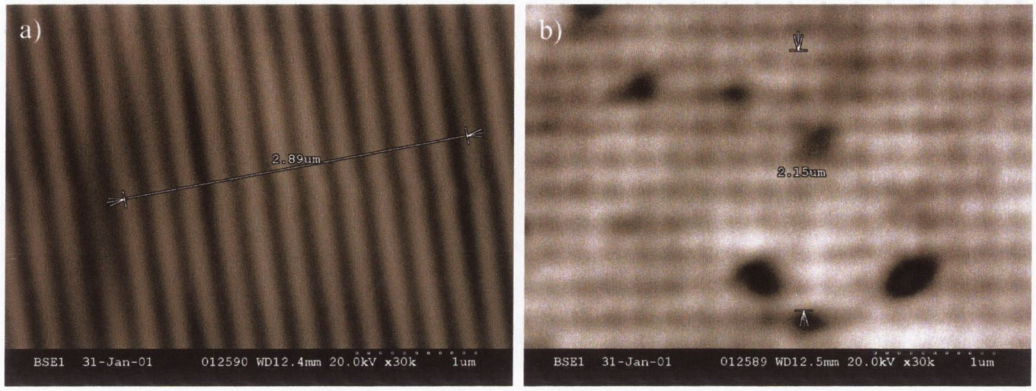

Figure 3.8: This shows a SEM scan of the cross-grating on the Ni substrate. The periodicity was measured to be 264nm

The functionality test of the shear-force system displayed good agreement to the samples used. Therefore we conclude that the shear-force system performs satisfactory.

3.1.2 Calibration of the Tube Scanner

To find a calibration for the X and Y component of the piezo-tube scanner we utilised various calibration grids. In total, there were three calibration gratings used; two cross-gratings and one line grating.

The first grating used for the calibration was a grating provided by DTH in Denmark [84]. It consists of two overlayed line gratings to form a cross grating structure on a nickel substrate. A SEM image of this grating can be seen in figure 3.8. The line periodicity was measured in the SEM to be $\sim$ 264 nm. It can be seen from the SEM image that while it is possible to image both line gratings simultaneously, it was not possible to bring them both into sharp focus.

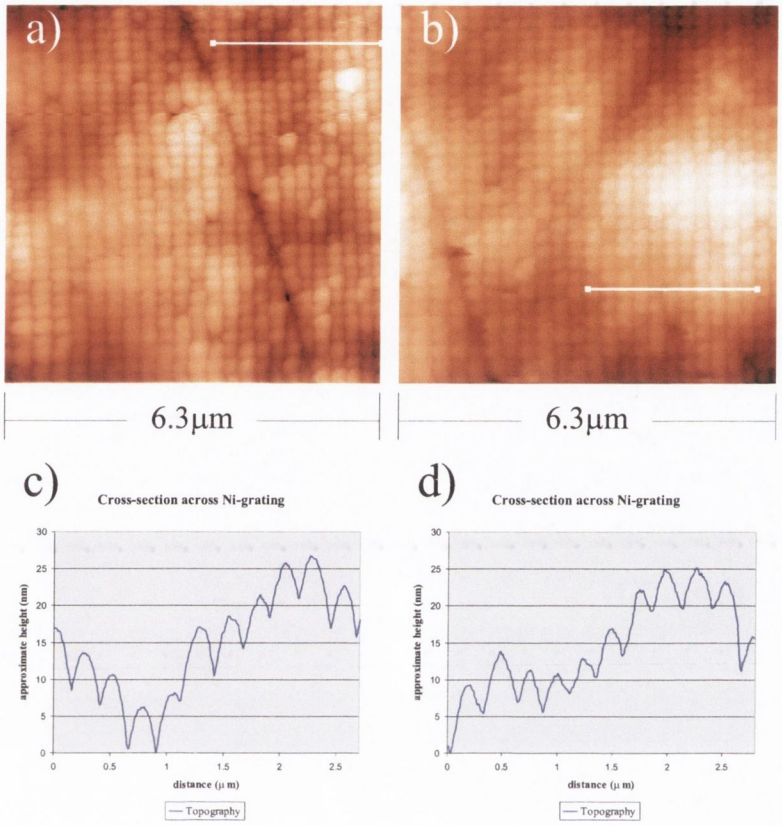

Figure 3.9: Scans a and b show the first results achieved on the cross-grating on Ni. The lines indicated on the images correspond to the cross-sections shown in graphs c and d. The scan size is approx. $(6.3\ \mu\text{m})^2$

This sample was then scanned with the SNOM/Shear-Force microscope and the following results were obtained. The first scans of this sample can be seen in figure 3.9a, b and cross-sections are shown in figure 3.9c, d. Taking these values into account showed that the maximum scan size achievable with the piezo-tube scanner is actually larger than expected. It was determined to be $\sim 9.3\ \mu\text{m}$.

To confirm this result, other grating samples were used. The first one

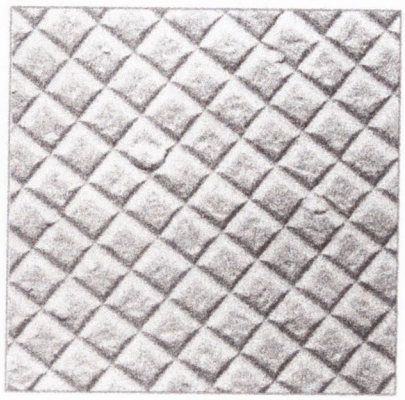

Figure 3.10: SEM scan of the grating sample from Agar Scientific. The lines are 463 nm spaced.

of these gratings is one commercially available from AGAR Scientific. It was originally made for the calibration of Transmission Electron Microscope (TEM), which requires the use of very thin samples. It is structured out of two overlayed samples, one coarse grating made from copper and one very thin carbon film with a cross grating of 2160 lines/mm (this corresponds to a 463 nm periodicity). A SEM image of this sample can be seen in figure 3.10. This sample presented some initial difficulties for scanning due to the softness (therefore being fragile) of the carbon grating. Figure 3.11 shows the shear-force scan of this grating as well as the cross-section of the scan. This result confirmed the calibration achieved by the previous grating to be correct.

The third grating used was a sample provided by the University of Nijmegen, Netherlands. It consisted of a chromium film evaporated on a substrate with laser focused nanofabrication. The film was evaporated while generating an interference pattern between two lasers (425.55 nm) above the

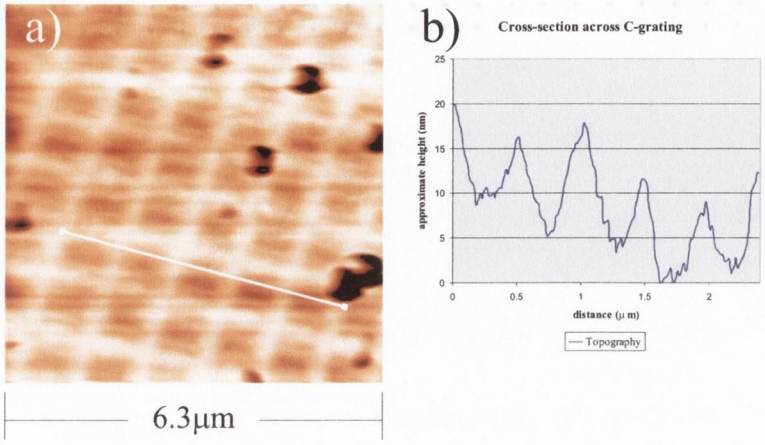

Figure 3.11: Shear-force image of the carbon grating as well as a cross-section. The result shows an agreement in between this result and the result on the previous grating. Scan size is $(3.1\ \mu\text{m})^2$

sample. The effect of this interference was to funnel the evaporated chromium into linetype structures with a spacing of 212.78 nm [85]. Due to the fact that the lines are created by using an optical system makes the line spacing as accurate as possible. This sample is actually the only real calibration sample used, it will be used as a standard calibration sample at National Institute of Standards and Technology (NIST). The results of shear-force scans on this sample can be seen in figure 3.12a and b, while cross-sections can be seen in figure 3.12c and d. On a large scale scan this is in good agreement with the previous results. When using the smaller scale scans this is not the case. The error is quite significant, which shows that it is necessary to have two different calibrations. One for the large scale and one for smaller scale scanning. This is due to hysteresis effects of the piezo tube.

This is not a major problem, due to the fact that the impedance ex-

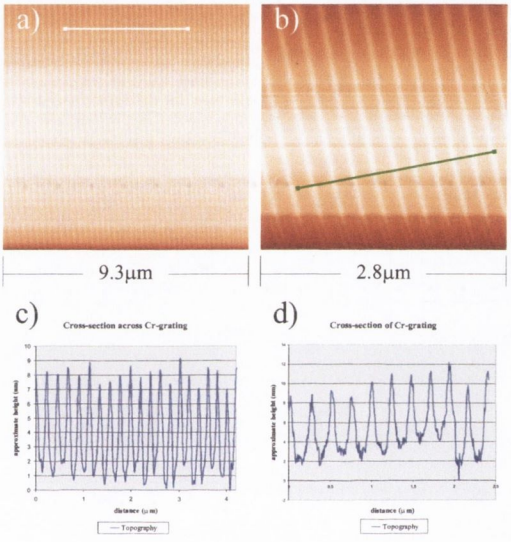

Figure 3.12: Shear-force scans of the Cr-line sample provided by the University of Nijmegen. Image (a) has a dimension of $(9.3\ \mu\text{m})^2$. Image (b) has a dimension of approx. $(2.8\ \mu\text{m})^2$. Graphs c and d show cross-section taken at the marked lines of scans a and b.

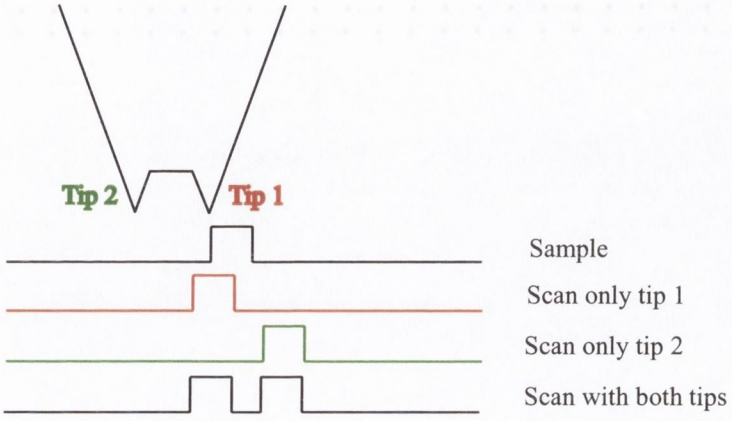

Figure 3.13: Graph shows a double tip and what type of image would be recorded with it. The red trace shows what the first part of the tip would record on its own. The green part shows the same for the second part. The trace below shows what the whole combination actually records in the end.

periments described later are based on very large scan areas. It is also not necessary to have accurate measurements due to the knowledge of the sample geometry from SEM scans. The error even in smaller scan ranges, is of the order of $\sim 5 - 10\%$, which is still acceptable in our case.

3.1.3 Double tip effect

During the initial shear-force testing a double tip effect artifact was observed. This so called "double-tip" happens when the probe has two sensing elements at the same distance away from the sample, while a "normal" probe only has one. This is illustrated in figure 3.13.

When only using one sensing element this would result in a normal topographic image. When using the second sensing element it would also show a standard topographic scan. The only difference compared to the image

Figure 3.14: This scan shows a shear-force scan of one of the test samples used. A double-tip effect occurred in this scan. The two sensing elements of the tip have a distance of approximately 1.4 μm.

taken with the first sensing element would be a offset between the two. But in the case of the double tip the sample is scanned with both sensing elements simultaneously, which results in an overlay of two topographic images taken with sensing element one and two respectively. The distance between the same feature on the image taken with the double-tip probe shows the distance between the sensing elements on the probe.

One of those shear-force scans can be seen in figure 3.14 with the features appearing twice with an offset of 1.4 μm. This shows that the distance between the two sensing elements was 1.4 μm in size.

This artifact has to be taken into account when interpreting the shear-force as well as the SNOM images.

3.2 Initial SNOM-Results and Z-calibration

After the initial testing of the shear-force feedback system and the calibration of the tube scanner in the X- and Y-directions, it was necessary to test the optical part of the SNOM/Shear-Force system, as well as calibrating the tube scanner in the Z-direction. This was done in a similar way to the tests of the shear-force system. First optical approach curves were investigated and used for calibration of the tube scanner in the Z-direction. After this initial one dimensional test it was necessary to perform optical scans with the shear-force feedback system in place. The SNOM was operated in this mode for the rest of the Project.

The optical scans were performed on a variety of samples, including some of the samples used for calibrating the shear-force system. Most of these initial results were obtained using non-coated tips, due to the larger signal achievable by the PMT and without polarisation control.

3.2.1 Optical Distance Curves and Z-calibration

The optical distance curves were performed by approaching a tip to the sample and simultaneously recording the reflected light from the sample. In our case, the sample was approached from out of contact (approximately 4.5 μm away from the sample) until the feedback system engaged and stopped the approach. One of these optical distance curves can be seen in figure 3.15.

It can be seen that at further distances from the sample the reflected light is nearly constant. As soon as the tip approaches contact (approx 3 μm) the signal starts to oscillate. These oscillations can be explained in terms of an interference effect with the reflected light. Due to the "width" of the tip

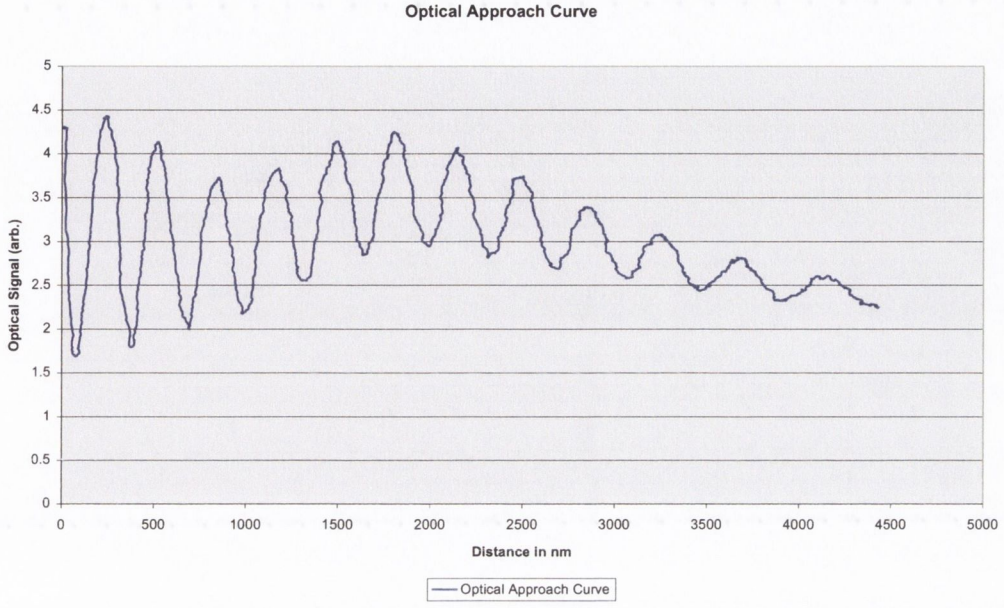

Figure 3.15: This graph shows an optical approach curve. It can be seen that at further distances from the sample the oscillation due to interference is low.

at the front (especially when tips with a thick Al coating are used) it can happen that some of the light undergoes multiple reflections between the tip and sample before detection. This light and the light directly reflected by the sample without the additional optical path can interfere in the far-field.

This information is very helpful in calibrating the tube scanner in the Z-direction. Using this information, it is clear that the difference the tube scanner has to travel in between two maxima is $\frac{\lambda}{2}$ (in our case 317.5 nm). The voltage required for the tube scanner to move this distance can then be measured along with the full Z range of the piezo tube. Taking the data in figure 3.15, this results in a maximum Z-range of 5.4 μm and a sensitivity of the scanner of $\sim 19.5 \frac{\text{nm}}{\text{V}}$.

Figure 3.15 also shows that a small movement in the z-direction can have a significant effect on the measured signal; a movement of 160 nm can result in a change in intensity of up to 50-150% (depending on whether the minimum or the maximum is seen as 100%). This corresponds to an average change of 2-8% per 5 nm, but due to the fact that it is a sinusoidal change this can be significantly larger. Taking into account that the effects which are investigated are only a fraction of the total signal detected shows the importance of maintaining the tip/sample distance as constant as possible, within 1nm or less. If this is not the case, artifacts can be observed. Some of these will be described later on in this chapter.

3.2.2 Initial SNOM results

After this one dimensional test it was necessary to prove that the system will also work in a two dimensional situation. To do this, some of the samples previously used for calibrating the system in the X- and the Y-direction and some new ones.

The first sample used to achieve optical results was the grating sample on a Ni-substrate. The sample itself was described in the Shear-Force section (figure 3.8). The results of this sample can be seen in figure 3.16.

A good correlation to the expected result can be seen. However, sometimes it seems to be difficult to image the horizontal and vertical lines at the same time. While doing the SEM characterisation it was also observed that it was not possible to have both sets of lines in total focus. It was possible for example, to image the vertical lines first and then by focusing on a different plane to image the horizontal lines. In between the focal planes of the

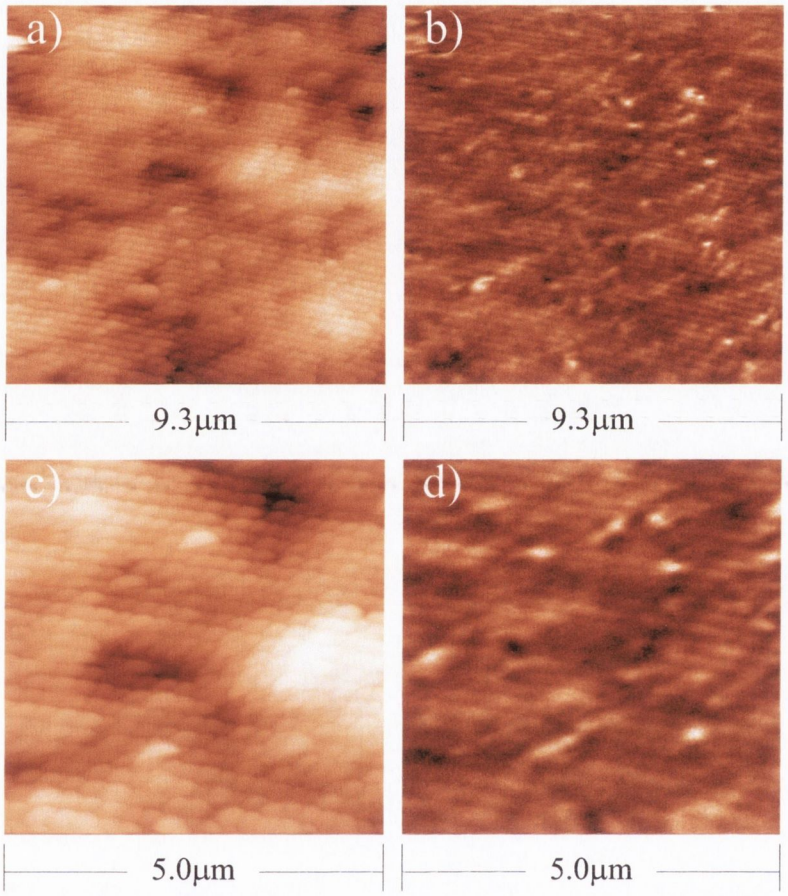

Figure 3.16: These are scans of the grating on a Ni-substrate. The line distance is approx. 264 nm. Images a and c show the topography and images b and d the optical scans. Scans a and b show an overview of a larger region ($(9.3\ \mu\text{m})^2$). Scans c and d show a zoom in of the centre portion of the first scan with a size of $(5\ \mu\text{m})^2$. A good correlation between the topographic and the optical images can be seen. It has to be noted that the horizontal lines are visible all over the sample, while the vertical lines are only visible in some areas.

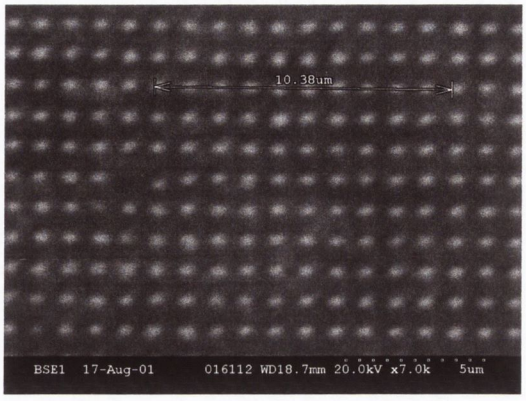

Figure 3.17: This SEM image shows Cr-dots on a glass substrate. The distance between the dots is of the order of 1 μm.

respective lines it was possible to image both sets of lines (figure 3.8b), but only in poor focus. This suggests that the lines are in two different layers and that the second layer (the lower layer of the two) is too far away to resolve simultaneously with the top layer. It was possible to image them in certain areas, but not necessarily on the whole scan. This could be due to the different thicknesses of the gratings.

The second sample used for SNOM testing was a dot-grating. The sample was part of a larger sample with various features that were used later on. It was provided by the University of Kassel and consisted of Cr-patterns on glass. The separation between the dots was approx. 1 μm in X and Y. A SEM image of this part of the sample with a distance measurement can be seen in figure 3.17.

When scanning this sample for the first time it was impossible to achieve a useful topographic image via shear-force. The recorded image looks basically flat. But when looking at the optical image achieved, it showed a

regular periodicity and a good correlation to the expected features. Due to the "non" existence of the topography this image was basically achieved in constant height mode. Constant height mode keeps the tip at a constant plane above the sample and does not vary the height when approaching topographic features. The other scans obtained during this study were usually performed in the constant signal mode, which varied the sample/tip distance when approaching topographic features, while keeping the Shear-Force signal constant. The optical image can be seen in figure 3.18. A cross-section is also shown, which shows the expected result. The advantage of using the shear-force detection in this mode is that the image is free of artifacts introduced by topographic coupling, which is discussed in the next section on other samples.

Two more features of the Cr on glass sample supplied by the University of Kassel were studied. The first were ring type structures etched into the Cr layer. The second were holes etched into the Cr layer. Closer SEM views of these features can be seen in figure 3.19, showing rings (a,b,c) and holes (d).

After mapping the sample with a SEM, it was necessary to compare this to the results achieved by using the SNOM/SF-Set-up. The second feature imaged from this sample were the ring type structures. They consisted of slotted rings in the Cr-layer on top of the glass substrate. Two types of rings were imaged. The first type is a ring with a diameter of $\sim$ 2.9 μm and a width of the ring wall of around 300 nm (top left image of figure 3.19, left array of rings). The second one imaged was smaller in diameter ($\sim$ 2.8 μm) but has a wider wall (900 nm) (array in the middle).

Images of the first type of rings can be seen in figure 3.20a-d. Clear

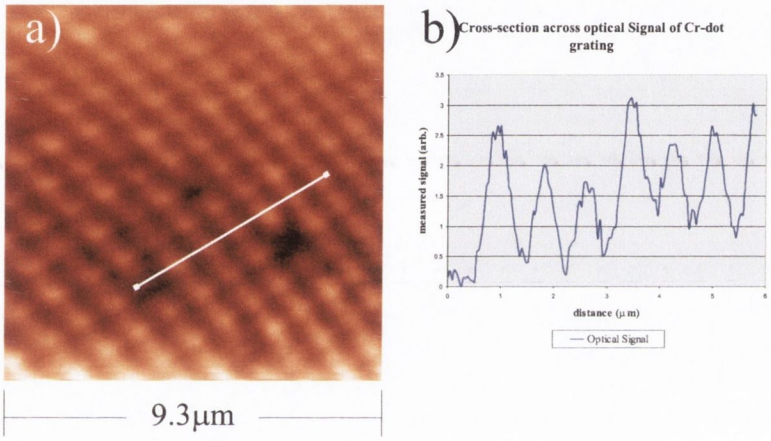

Figure 3.18: The SNOM scan (a) shows the Cr-dots on glass. The dot spacing is in agreement with the SEM image. Due to problems with the Shear-Force during this scan, which resulted in a constant height scan, the result is not affected by topographic artifacts. Graph b shows a cross-section taken along the line marked in scan a.

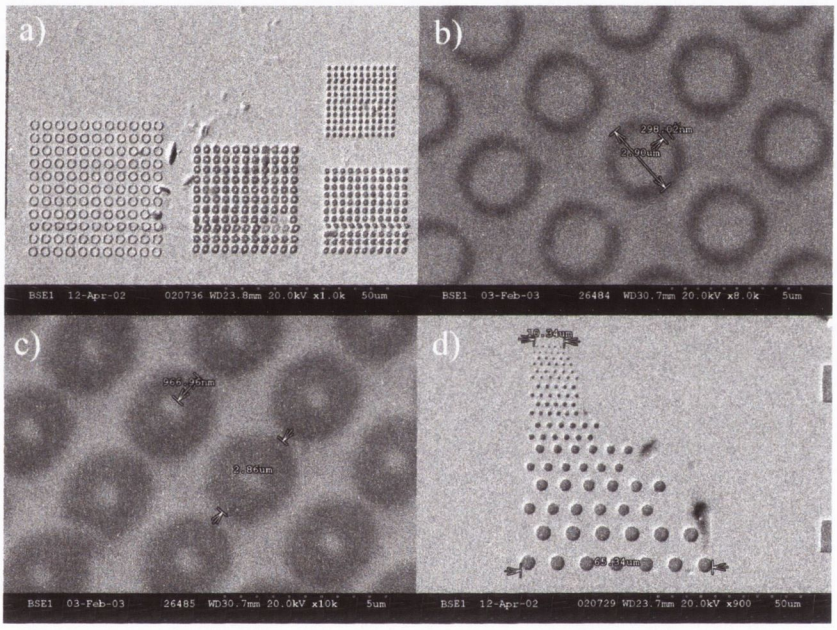

Figure 3.19: These SEM scans show zoom-ins on the areas studied. Image a, b and c show the slotted ring structures. Image d shows the holes.

correlation between the Shear-Force topography image and the optical image can be seen. The size of the features correspond to the expected value, as imaged with the SEM. One interesting aspect of the optical image b is that the intensity varies across the ring. All of the rings in this scan seem to have a maximum intensity at 45° and 225°, while they appear to have a minimum at 135° and 315°. This can be seen when taking a "cross-section" around the ring structure, shown in figure 3.20 e. It shows the change of the two maxima at 45° and 225° and the minima at 135° and 315°. The change of optical signal in between a maximum and a minimum is approximately a factor of 10.

Similar results were observed by Betzig et al [86] when ring type structures (metal rings on glass) were observed with polarised light in transmission and reflection. They also observed a change in intensity depending on the polarisation direction of the light used for illumination.

In our case, the polarisation control was not in place at the time of this experiment and we had no means to polarise the light in a controlled fashion.

When looking at the second set of scans of figure 3.20 (c,d) no intensity change can be seen. The same can be seen when looking at the cross-section around the ring in figure 3.20 f. This suggests that the tip used to image figure 3.20(a,b) had a preferred polarisation direction, while the one used to image scan (c,d) had non.

The second set of rings can be seen in figure 3.21. No change in intensity could be seen there. The reason for this could be that the tip had no preferred polarisation or the size of the ring walls. The topography scan shows a good correlation with the optical scan. The optical scan is inversed to the

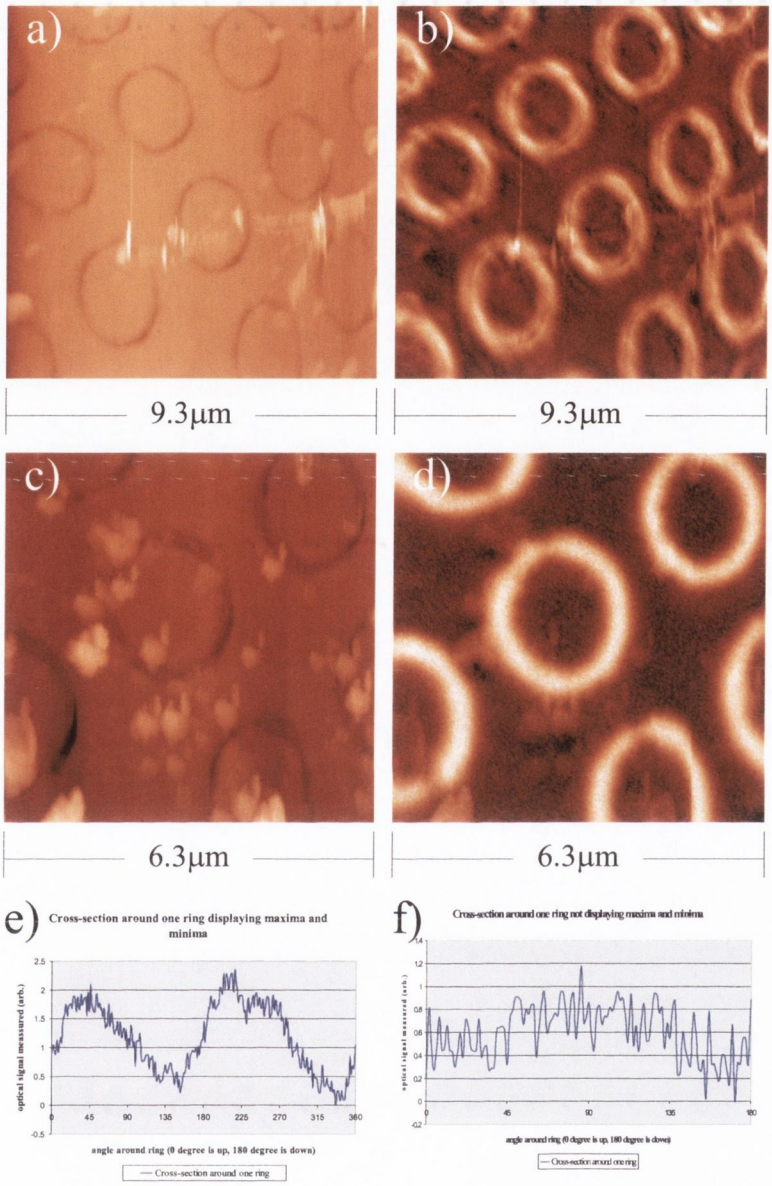

Figure 3.20: Two scans of the first type of rings can be seen here. The left shows the topography and the right shows the optical image. The top scan has a dimension of $(9.3\ \mu\text{m})^2$. The bottom scan is a zoom in on the same array, the size is $(6.3\ \mu\text{m})^2$. Cross-sections seen in graphs e and f were taken around the ring for graph e or half way around the ring for graph f.

topography, imaging the glass part as a brighter area than the Cr part.

The next feature were the holes marked area 3. The SEM image of them can be seen in figure 3.19b. They are also etched into the Cr-layer on glass and therefore the interior of the holes consists of glass and the external material is the Cr-layer, the diameter of them is ~ 2.6 μm. Scans of these holes with the SNOM/Shear-force set-up can be seen in figure 3.22. Higher magnifications of them can also be seen (figure 3.22c,d), showing the grains of the glass or remaining Cr in the hole area. This can not only be seen in the topography but also in the optical scan. This suggests a resolution of better than 60 nm in the optical signal for this tip/sample combination.

The final sample imaged without polarisation control was the sample provided by the University of Cambridge which consisted of the transmission lines used later on for the polarisation experiments for impedance matching. The specific design will be discussed in more detail in the next chapter on the polarisation results and can be seen there in figure 4.3.

The part with varying width between the transmission lines was imaged without polarisation control in place and can be seen in figure 3.23. It shows a good agreement between the expected result and the optical and shear-force scan. One interesting effect seen on these scans are the bright edges around the lines. This effect will be discussed in more detail in the next section on SNOM artifacts.

3.2.3 SNOM artifacts

Two artifacts of SNOM images were also observed during this PhD study. Both of them were mainly due to topographic features on the sample and

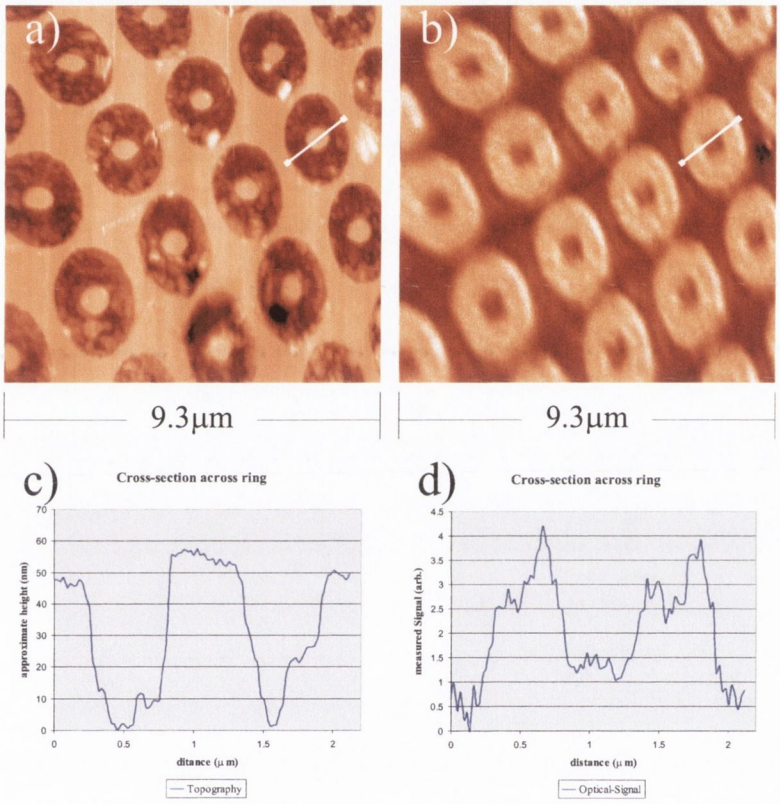

Figure 3.21: The scan of the second set of rings shows a good agreement to the expected results. The size of the scan is $(9.3\ \mu\text{m})^2$. Image a shows the topography and image b the optical image. The cross-sections underneath (c,d) were taken at the marked areas respectively. They show that the glass part of the sample is imaged with a higher intensity than the Cr parts.

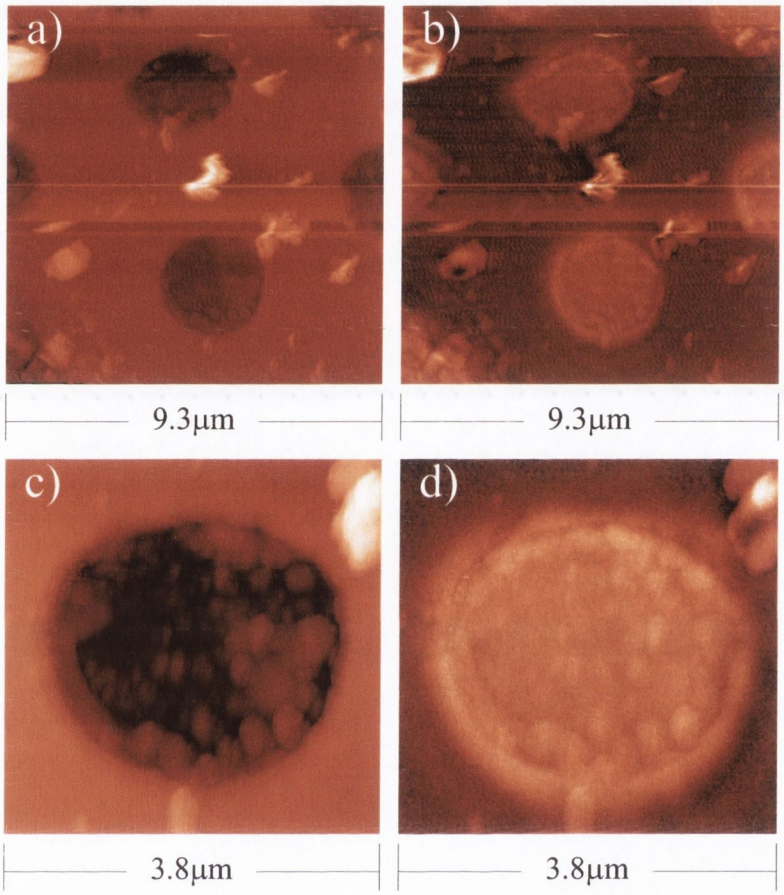

Figure 3.22: The holes in the chromium layer can be seen in these two scans. The scans a,c show the topography and b,d the optical image. Scans a,b is an overview scan ($(9.3\ \mu m)^2$) and scan c,d is a zoom in ($(3.8\ \mu m)^2$) on the lower hole seen in the overview. In scans c and d small grains in the glass can be seen in the topography as well as the optical image.

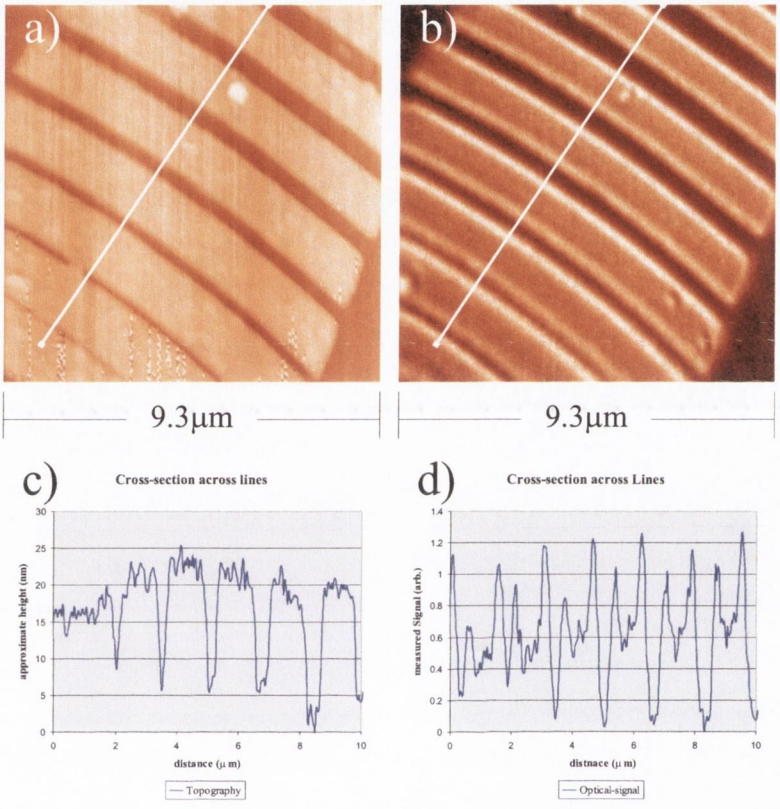

Figure 3.23: This shows a scan of the sample prepared by the University of Cambridge and used in the next chapter for the polarisation experiments. The size of the scan here is $(9.3\ \mu\text{m})^2$. Scan a shows the topography and scan b the optical image. Graphs c and d show cross-section of the lines marked on the respective image. One interesting aspect of the optical image is the bright lines along the edge of the lines. This can be explained by shadowing effects.

would not be visible on a homogeneous flat sample.

Shadowing at Topography edges

The first artifact is the observation of bright edges along topographic features. This artifact could be especially well seen when imaging the sample provided by the University of Cambridge. This is due to the sharp step edge when looking at the profile of this sample; 20 nm height from top of the line to the substrate in the gap.

When the tip is above a flat part of the sample, a large amount of the reflected light will be shadowed by the tip and will not be detected. Due to the broad size of the tip when the aluminium coating is taken into account, this amount of shadowed light is quite significant when the scanning height is approximately 5 nm and the tip width is up to 250 nm. This results in a "direct" collection angle of only 4.6°. Some more light can be detected by being reflected by the sample to the tip and back to the sample before it gets collected in the far-field.

When the tip reaches the stepedge of a topographic feature, this changes the amount of light shadowed by the tip itself. The distance between the tip and the sample is then much larger; nearly 30 nm for part of the sample area that reflects the light. This results in a collection angle of 13.5° for direct collection and also the rereflected amount collected is larger. A sketch of this can be seen in figure 3.24

To calculate the angles it was assumed that the light is coming out of the centre of the tip. It is then illuminating the sample and is reflected to the collector. To get direct detection it is necessary that the reflected light passes

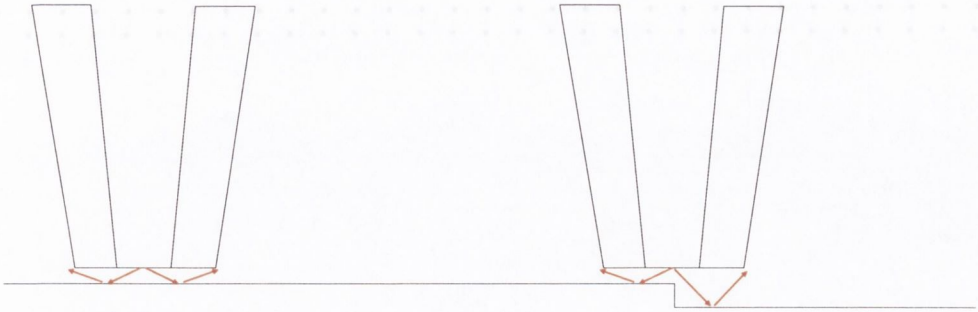

Small amount of light detected directly without being shadowed by the tip.

Larger amount of reflected light can be collected without being shadowed by the tip.

Figure 3.24: This sketch illustrates what happens when the tip is over a flat area or over a step edge. When it reaches a step edge part of the light transmitted by the tip will be reflected from the sample substrate (i.e. the lower part of the step), therefore increasing the angle for direct collection of the light.

the edge of the tip without being reflected by it. This can be expressed as

$$\theta = atan\left(\frac{d}{r/2}\right) \tag{3.2}$$

with distance d and the radius of the tip r. The principle behind this is the one used in linear optics as incident angle is equal to reflection angle.

This would explain the increased intensity at the line edges. As soon as the tip moves into the gap, the feedback reduces the distance to the standard value of between 2-10 nm.

Interference Imaging

As already shown in the introduction, some scans displayed two overlayed images, one with a high resolution and another one with low resolution. This was also observed by Betzig et al [35] and may be explained by interference effects. The problem of this artifact, especially with reflection mode SNOM set-ups, is that the intensity is highly dependent on the distance between the tip and the sample. This can be seen from the optical approach curves (figure 3.15). The intensity changes while approaching the sample in a periodic fashion. The distance between two adjacent maxima is $\frac{\lambda}{2}$. This therefore suggests that an interference phenomenon occurs.

When the tip undergoes small movements away from the sample (in the region of 5nm) this can have a significant effect onto the optical signal. The change can be up to 5-10%. With such a large change the problem is that the near-field signal is smaller than the signal change. Because of this a high resolution image is created which is only related to the topography. This image will show the exact same resolution as the shear-force scan.

The actual optical image is visible as well, but with a much lower resolution. This can be seen in figure 1.7. Features visible in the topography and shear-force image with the same resolution are marked with cyan arrows, while the gap in the "real" optical image are marked with yellow arrows.

Both of these artifacts, as well as the artifact discussed in the shear-force section have to be taken into account when interpreting SNOM/shear-force scans. And it can be seen that it is therefore very important to record the topography image when a feedback system is used.

Chapter 4

Polarisation Mode SNOM Results

This chapter deals with the results achieved with polarisation control in place. The first part of the chapter gives a short introduction to how the polarisation was measured and the setup for the experiments. It will also show a typical chart for the extinction ratio of the polarisation. The second part of the chapter then concentrates on the continuation of polarisation experiments on transmission type-like structures. Impedance matching is discussed as one of the possible explanations for the observed polarisation induced effect. A short introduction to impedance matching and impedance calculations is given, before showing the results on variable impedance samples. The impedance calculations are used to give approximate values for the impedance values of the transmission lines as well as the tip.

4.1 Polarisation control

For the following experiments it was necessary to vary the polarisation of the light from the tip in a controlled manner.

This was done by measuring the polarisation in the far field with the help of an analyser. The polarisation was controlled in the following way. Before coupling the light into the fibre the polarisation was altered. It was first prepolarised by a standard sheet polariser (Melles Griott). After this a half-wave plate (CVI Laser) and then a quarter-wave plate (CVI Laser) were used to control the polarisation direction.

For most of the experiments it was only necessary to get a polarisation rotation by 90°, to image the transmission lines with TM- or TE-polarised light in respect to the transmission lines. The analyser was placed between the tip and a telescope or a PMT. The analyser was then set 90° to the desired position and the polarisation was varied by the wave plates to achieve maximum extinction. It was then possible by replacing the telescope with the PMT to measure the extinction ratio achieved by taking measurements with different analyser settings. The procedure was repeated for the polarisation in the perpendicular setting. In this way, it was possible to change the polarisation between the two settings by adjusting the wave plates to the required values between two scans.

It was not possible to polarise some of the tips in different directions. These tips could not be used in the initial stages of the polarisation experiments. One reason for this pre-polarisation behaviour could be an elliptical aperture shape and therefore a preferred polarisation direction of the light transmitted through the aperture.

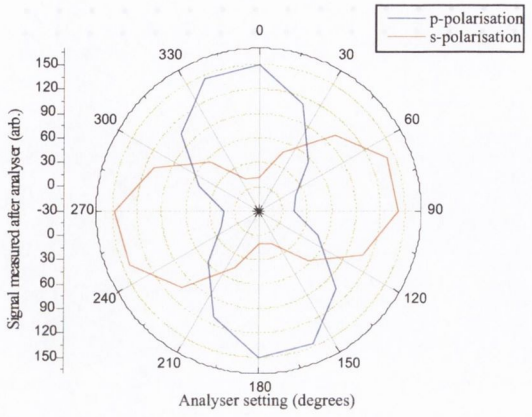

Figure 4.1: A plot of the values measured with a PMT when the analyser is placed in between the tip and the PMT. Two settings were achieved, s- and p-polarisation. The extinction ratio in both of these two cases was approximately 20:1.

A typical graph showing the polarisation of a tip with good polarisation characteristics in two perpendicular directions can be seen in figure 4.1. This graph shows a typical extinction ratio (20:1) achieved with the described set-up. Figure 4.2 shows a similar graph, but in this case it was only possible to achieve a good polarisation characteristic in one direction, the extinction ratio in this case is 20:1. In the perpendicular direction the signal is very weak overall and the extinction ratio is only 4:1.

In general, an extinction ratio as high as 50:1 and as low as 2:1 or less was obtained. Extinction ratios of up to 2000:1 were reported by other groups [86], but could not be reproduced.

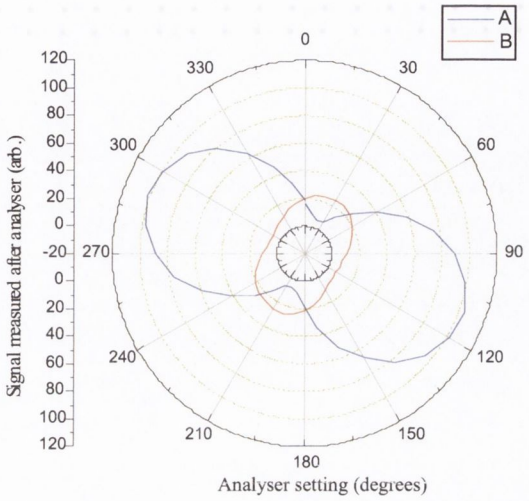

Figure 4.2: A plot of the signal measured with an analyser between the tip and the PMT. A good extinction ratio as well as a good signal level are achieved along direction A, but not in the perpendicular direction B.

4.2 Impedance Matching Experiments

The plan of the experiment performed was to further investigate the polarisation effect on transmission type like structures shown in chapter 1.4. One of the possible explanations brought forward was impedance matching due to the close resemblance of both structures (probe and sample) with standard microwave components (circular waveguide and coplanar transmission line). The further investigation is presented here.

4.2.1 Impedance Samples

For experiments taking the impedance matching into account, it was necessary to produce samples with different impedance values, ideally within the scan range of approximately 10 μm $\times$ 10 μm.

We have decided to use samples forming coplanar transmission lines for the reason that the parameters which change the impedance of coplanar striplines or coplanar waveguides are: the dielectric constant of the substrate, the thickness of the substrate, the width of line and the width of the gap between the lines.

Taking into account that different impedance values should be visible in one scan disqualifies the first two parameters. This leaves two possibilities with either the gap-width or the line-width staying the same and the other being changed. The decision was made to keep the line-width the same and vary the gap in between. This was partly due to the way the samples were made. The samples were prepared by evaporating Cr or Au onto a pattern produced by e-beam lithography on a photoresist.

Coplanar transmission lines are also routinely used in microwave theory and therefore existing formulas can be used to approximate the impedance values.

A sketch of the sample prepared can be seen in figure 4.3. It consists of two parts. The first part is a set of lines with a line width of 1 μm and a gap width of 250 nm. The second part consisted of the same type of lines as the first one (1 μm width) but the gap width between the lines varied between 200 nm and 1 μm, changing in 100 nm steps. Both structures were produced twice on a 30 μm $\times$ 30 μm area (biggest achievable with the TEM) rotated by 90° to each other. This was done so that imaging with different polarisations could be compared on the sample structures without changing the polarisation direction of the tip.

The sample pattern was produced on different types of substrates (Glass,

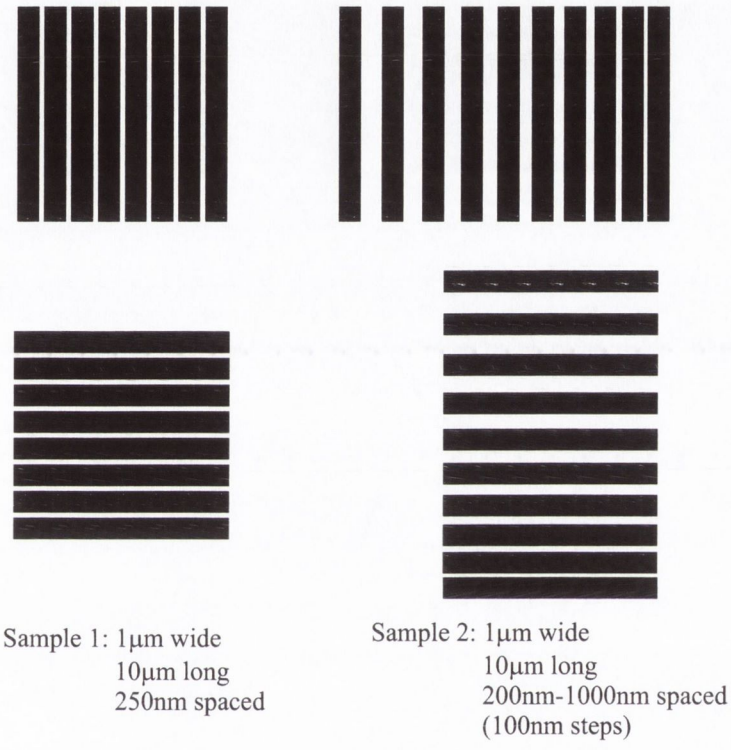

Figure 4.3: Sketch of the pattern produced by e-beam lithography on different substrates. It consists of two parts. The first part (seen on the left) is a set of lines with a line width of 1 μm and a gap width of 250 nm. The second part (seen on the right) is the part with variable impedances. In this case the line width stays the same, and the gap width changes between 200 nm -1 μm in 100 nm steps.

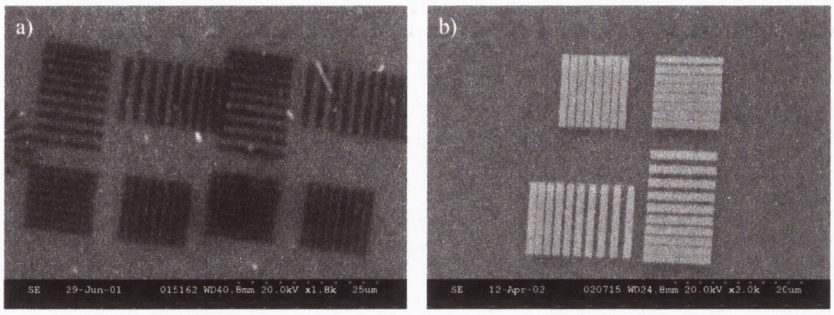

Figure 4.4: The sample of figure 4.3 imaged in a SEM.

Si Quartz and $SrTiO_3$) and with different type of metals (Cr and Au). The results shown here were mainly achieved on the Si sample with Au lines. The thickness of the metal evaporated was 20 nm (measured by a Quartz-Crystal monitor). SEM images of this sample can be seen in figure 4.4.

4.2.2 Equally spaced lines

The sample used is the part shown on the left in figure 4.3 and consists of an array of 1 μm wide and 250 nm spaced lines. This part of the sample was imaged with TM and TE polarised light to see if the contrast reversal could be achieved.

The results are shown in figure 4.5. This figure shows the equally spaced line array imaged with TM and TE polarised light (figure 4.5a, b respectively). A clear contrast reversal between the two images can be seen. The image taken with TM polarised light shows the lines as bright and the gap as dark, while the image taken with TE polarised light shows the lines as dark and the gap as bright. This can be more clearly seen when looking at the cross-section in figure 4.5c.

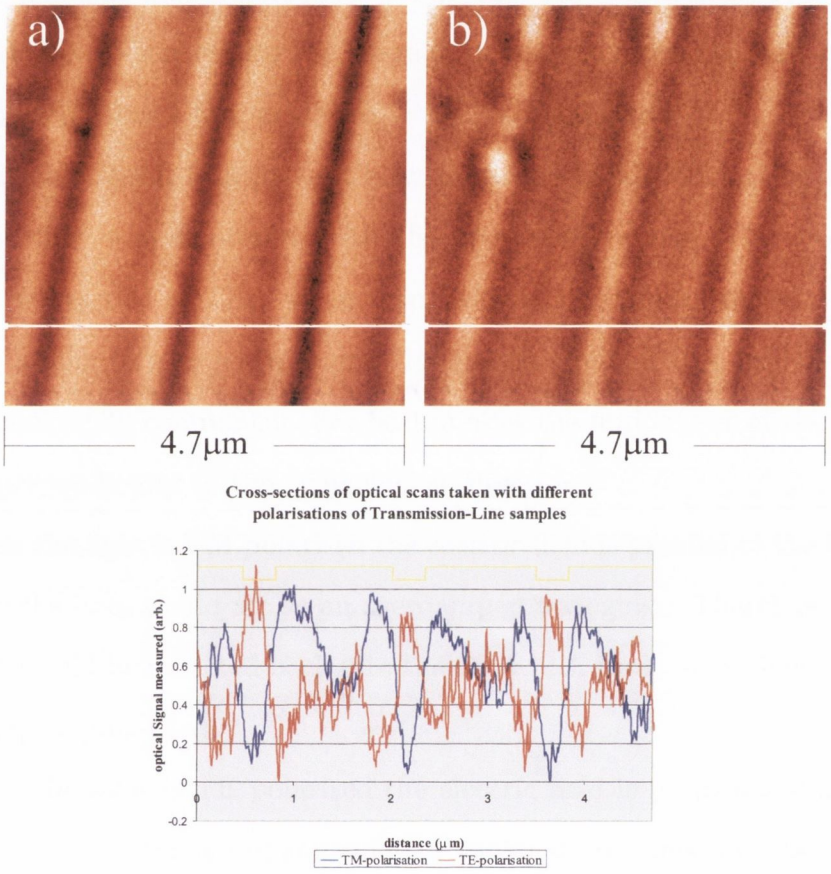

Figure 4.5: SNOM scans taken with different polarisations from the same sample region. Image (a) shows the scan taken with TM polarised light. Image (b) is taken with TE polarised light and shows the contrast reversal. The scan size is $(4.7\ \mu\text{m})^2$. Graph (c) shows a representative cross-section at the markings shown in scan (a) and (b).

It also has to be noted that the actual effect takes place in the gap and not on the lines. When comparing the average of the centre part of the lines from both TM and TE scan only a minor difference of intensity (~10%) can be registered. When taking the average intensity in the gap and compare them to each other a change of ~70% can be registered.

To explain this it is important how the electric fields look at the aperture and how they would interact with the imaged structures. The mode in a circular waveguide is TE_{11} when using ideally conducting metals and the coating is infinitely large. In reality the aperture of the fibre probe also has a HE_{11} mode [29] component. For both modes the major part of the electric field is perpendicular to the propagation direction.

When the light is TM polarised the electric field is parallel to the lines. In this case the lines would act as an overdamped waveguide. Therefore most of the light would be reflected back into the tip, which leads to the low intensity in the gap (figure 4.5a).

When the light is TE polarised the electric field is perpendicular to the lines. In this case the dominant mode of coplanar transmission lines (TEM) can be excited. The TEM mode does not have a cut-off frequency. This would favour that the light would exit the tip rather than being reflected back into it. This explains the higher intensity detected in the gap (figure 4.5b) when compared to the image taken with TM polarised light.

4.2.3 Impedance matching

Impedance matching is a standard technique used in microwave engineering. Matching networks are used in microwave circuits for better power transfer

between different circuit areas. It is used when two different parts of a circuit with different impedance values have to be connected. The amount of the total energy transfer/loss is dependent on the mismatch between the two different circuit areas. When the impedances of the two sections match the maximum power will be transfered. If the mismatch is large, energy transfer will be low and some of the energy will be reflected back to the source. It is therefore necessary to have good matching between circuit areas to ensure the maximum transfer and minimum loss of energy.

Our intention was to establish if a similar effect can be achieved in optics. The system consists of two parts as well. The coupling takes place between the probe that can be modelled as a circular waveguide and the structures printed on the substrate. They can be modelled either as a coplanar stripline or a coplanar waveguide. Neither of these two models will suit perfectly as will be seen later on, but the actual value will be somewhere in between the two.

In the following subsection we calculate the impedances of these structures. All the calculations are approximations using the formulas for much lower frequencies than the ones used for the experiments performed. Therefore they can only be used as guidelines and not as quantitative figures for the observed behaviour. For more in detail calculations it would be necessary to use numerical methods to achieve quantitative numbers for the impedance values of the different structures.

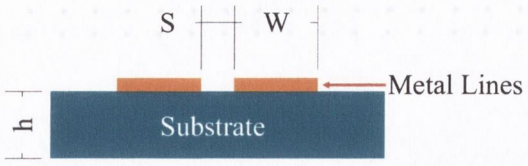

Figure 4.6: This sketch show a cross-section of a coplanar stripline. S is the size of the gap width, W is the size of the metal line and h is the thickness of the dielectric substrate.

Coplanar Stripline

Coplanar stripline consists of two parallel lines of the same dimension (width and thickness) separated by a gap. The two lines are printed on a dielectric substrate. A sketch of this structure can be seen in figure 4.6

The dominant mode supported by coplanar striplines is a quasi-TEM mode. This mode does not have a cut-off frequency, which makes it more favourable than any of the other modes in our case. The characteristic impedance is:

$$Z_0 = \frac{120 \cdot \pi}{\sqrt{\epsilon_e}} \frac{K(k)}{K(k')} \tag{4.1}$$

The effective dielectric constant ϵ_e is:

$$\epsilon_e = 1 + \frac{\epsilon_r - 1}{2} \frac{K(k')K(k_1)}{K(k)K(k_1')} \tag{4.2}$$

with $k = \frac{a}{b}$, $a = \frac{S}{2}$, $b = \frac{S}{2}+W$, $k' = \sqrt{1-k^2}$ and $k_1 = \frac{\sinh\left(\frac{\pi \cdot a}{2 \cdot h}\right)}{\sinh\left(\frac{\pi \cdot b}{2 \cdot h}\right)}$. S corresponds to the gap width, while W represents the width of one of the transmission lines. h is the thickness of the dielectric substrate and ϵ_r is the dielectric constant of the substrate.

$$\frac{K(k)}{K'(k)} = \begin{cases} \left[\frac{1}{\pi} \cdot \ln\left(2\frac{1+\sqrt{k'}}{1-\sqrt{k'}}\right)\right]^{-1} & 0 \leq k \leq 0.7 \\ \\ \frac{1}{\pi} \cdot \ln\left(2\frac{1+\sqrt{k'}}{1-\sqrt{k'}}\right) & 0.7 \leq k \leq 1 \end{cases} \tag{4.3}$$

with $K'(k) = K(k')$.

These formulas can now be used to calculate the impedance values for the dimensions of the samples used. First k has to be calculated to decide which part of formula 4.3 has to be used.

$$k = \frac{a}{b} = \frac{\frac{S}{2}}{\frac{S}{2}+W} = \frac{S}{S+2\cdot W} \qquad \begin{array}{l} 200nm \leq S \leq 1\mu m \\ W = 1\mu m \end{array}$$

$$\Rightarrow k \leq 0.7$$

Therefore 4.3 becomes:

$$\frac{K(k)}{K(k')} = \left[\frac{1}{\pi} \cdot \ln\left(2 \cdot \frac{1+\sqrt{k'}}{1-\sqrt{k'}}\right)\right]^{-1} \tag{4.4}$$

For k_1 we get

$$k_1 = \frac{\sinh\left(\frac{\pi \cdot a}{2 \cdot h}\right)}{\sinh\left(\frac{\pi \cdot b}{2 \cdot h}\right)} \Rightarrow k_1 = \frac{e^{\frac{\pi \cdot a}{2 \cdot h}} - e^{-\frac{\pi \cdot a}{2 \cdot h}}}{e^{\frac{\pi \cdot b}{2 \cdot h}} - e^{-\frac{\pi \cdot b}{2 \cdot h}}}$$

Using the values for this experiment we get

$$0 \leq k_1 \leq 0.7$$

Therefore the same part of equation 4.3 is used as above.

For the effective dielectric constant we get:

$$\begin{aligned}
\epsilon_e &= 1 + \frac{\epsilon_r - 1}{2} \cdot \frac{K(k')}{K(k)} \cdot \frac{K(k_1)}{K(k_1')} \\
&= 1 + \frac{\epsilon_r - 1}{2} \cdot \frac{1}{\pi} \cdot \ln\left(2 \cdot \frac{1+\sqrt{k'}}{1-\sqrt{k'}}\right) \frac{1}{\frac{1}{\pi} \cdot \ln\left(2 \cdot \frac{1+\sqrt{k_1'}}{1-\sqrt{k_1'}}\right)} \\
&= 1 + \frac{\epsilon_r - 1}{2} \cdot \frac{\ln\left(2 \cdot \frac{1+\sqrt{k'}}{1-\sqrt{k'}}\right)}{\ln\left(2 \cdot \frac{1+\sqrt{k_1'}}{1-\sqrt{k_1'}}\right)}
\end{aligned}$$

k' for $S = 200$ nm is $\Rightarrow k' = .9959$

k_1' for $S = 200$ nm is $\Rightarrow k_1' = 1$ for $h = 20$ nm or $k_1' = .9959$ for $h = 1$ mm. Using these numbers we get for ϵ_e:

$$\Rightarrow \epsilon_e = \frac{\epsilon_r + 1}{2} \tag{4.5}$$

Using formula 4.1 we get the following formula for the characteristic impedance:

$$\begin{aligned}
Z_0 &= \frac{120 \cdot \pi}{\sqrt{\epsilon_e}} \cdot \frac{1}{\frac{1}{\pi} \ln\left(2 \cdot \frac{1+\sqrt{k'}}{1-\sqrt{k'}}\right)} \\
&= \frac{120 \cdot \pi^2}{\sqrt{\epsilon_e} \cdot \ln\left(2 \cdot \frac{1+\sqrt{k'}}{1-\sqrt{k'}}\right)}
\end{aligned} \tag{4.6}$$

Now the k' values have to be calculated and can be put into equation 4.6. The resulting equation shows the characteristic impedance for this gap width divided by the effective dielectric constant.

Using equation 4.6 with the gap dimensions of the sample used results in the following formulas shown in table 4.1. These formulas are only dependent on the effective dielectric constant of the substrate.

To use the formulas of table 4.1 for our sample it is necessary to know the dielectric constant for Si. The value found in a table for dielectric constants

Table 4.1: Impedance of coplanar striplines for different gap width.

gap width in nm	value for k'	general formula for Impedance
200	.9959	$Z_{0,200} = \frac{156.57\Omega}{\sqrt{\epsilon_e}}$
250	.9938	$Z_{0,250} = \frac{165.39\Omega}{\sqrt{\epsilon_e}}$
300	.9915	$Z_{0,300} = \frac{173.21\Omega}{\sqrt{\epsilon_e}}$
400	.9860	$Z_{0,400} = \frac{186.75\Omega}{\sqrt{\epsilon_e}}$
500	.9798	$Z_{0,500} = \frac{198.35\Omega}{\sqrt{\epsilon_e}}$
600	.9730	$Z_{0,600} = \frac{208.58\Omega}{\sqrt{\epsilon_e}}$
700	.9658	$Z_{0,700} = \frac{217.80\Omega}{\sqrt{\epsilon_e}}$
800	.9583	$Z_{0,800} = \frac{226.20\Omega}{\sqrt{\epsilon_e}}$
900	.9506	$Z_{0,900} = \frac{233.94\Omega}{\sqrt{\epsilon_e}}$
1000	.9428	$Z_{0,1000} = \frac{241.14\Omega}{\sqrt{\epsilon_e}}$

was $3.2 \leq \epsilon_r \leq 4.7$. Table 4.2 shows three impedance values, one for the dielectric constant of $\epsilon_r = 3.2$, one for the dielectric constant of $\epsilon_r = 4.7$ and one is the mean value of the two.

Coplanar Waveguide

The other option is to describe the transmission line used as a coplanar waveguide. In this case, one line in the middle is separated by two identical gaps from two infinite size planes left and right of it. It is also printed on a dielectric substrate. A sketch of this structure can be seen in figure 4.7.

The dominant mode support by this structure is also a quasi-TEM mode, the same as with the coplanar stripline. This mode has no cut-off frequency and therefore it is the most favourable one. The characteristic impedance is:

Table 4.2: Impedance value for coplanar striplines on a Si substrate.

size of gap in nm	Impedance for $\epsilon_r = 3.2$ (in Ω)	Impedance for $\epsilon_r = 4.7$ (in Ω)	Mean of Impedance (in Ω)
200	108.04	92.74	100.4
250	114.13	97.97	106.1
300	119.53	102.60	111.1
400	128.87	110.62	119.7
500	136.87	117.49	127.2
600	143.93	123.55	133.7
700	150.30	129.01	139.7
800	156.09	133.99	145.0
900	161.43	138.57	150.0
1000	166.40	142.84	154.6

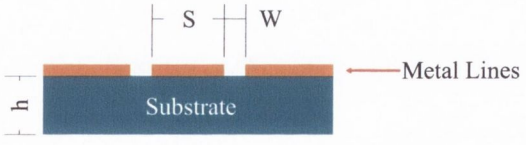

Figure 4.7: This sketch show a cross-section of a coplanar waveguide. W is the size of the gap width (left and right gap), S is the size of the metal line in the middle and h is the thickness of the dielectric substrate.

$$Z_0 = \frac{30 \cdot \pi}{\sqrt{\epsilon_e}} \frac{K(k')}{K(k)} \tag{4.7}$$

In this case, S is the width of the line in the middle, while W is the width of the two gaps. The equations for ϵ_e, $\frac{K(k)}{K'(k)}$ stay the same as for the coplanar stripline.

It now has to be decided again which part of formula 4.3 has to be used. For the dimensions on this sample k is between $0 \leq k \leq 0.7$ in all cases but the one for 200 nm. This results in using formula 4.4 for all the gap width except the one for 200 nm in which case formula 4.3 will be:

$$\frac{K(k')}{K(k)} = \frac{1}{\pi} \cdot \ln\left(2 \cdot \frac{1+\sqrt{k'}}{1-\sqrt{k'}}\right) \tag{4.8}$$

Going through the calculations as above results in two equations for the characteristic impedance. The first one for all gap widths (250 nm - 1000 nm) except for 200 nm is:

$$\begin{aligned} Z_0 &= \tfrac{30\cdot\pi}{\sqrt{\epsilon_e}} \cdot \tfrac{1}{\pi} \cdot \ln\left(2 \cdot \tfrac{1+\sqrt{k'}}{1-\sqrt{k'}}\right) \\ &= \tfrac{30}{\sqrt{\epsilon_e}} \cdot \ln\left(2 \cdot \tfrac{1+\sqrt{k'}}{1-\sqrt{k'}}\right) \end{aligned} \tag{4.9}$$

For the separation of 200 nm the characteristic impedance is:

$$\begin{aligned} Z_{0,200} &= \tfrac{30\cdot\pi}{\sqrt{\epsilon_e}} \cdot \frac{1}{\frac{1}{\pi}\cdot\ln 2\cdot\frac{1+\sqrt{k'}}{1-\sqrt{k'}}} \\ &= \tfrac{30\cdot\pi^2}{\sqrt{\epsilon_e}} \cdot \frac{1}{\ln 2\cdot\frac{1+\sqrt{k'}}{1-\sqrt{k'}}} \end{aligned} \tag{4.10}$$

Now $k' = \sqrt{1 - \frac{a^2}{b^2}}$ has to be calculated for various gap widths. The results for this and the general formulas, which only depend on the dielectric constants for the impedance values, can be seen in table 4.3

Table 4.3: Impedance of coplanar waveguides for different gap width.

gap width in nm	value for k'	general formula for Impedance
250	.745	$Z_{0,250} = \frac{99.12\Omega}{\sqrt{\epsilon_e}}$
300	.781	$Z_{0,300} = \frac{104.34\Omega}{\sqrt{\epsilon_e}}$
400	.831	$Z_{0,400} = \frac{113.03\Omega}{\sqrt{\epsilon_e}}$
500	.866	$Z_{0,500} = \frac{120.57\Omega}{\sqrt{\epsilon_e}}$
600	.891	$Z_{0,600} = \frac{127.23\Omega}{\sqrt{\epsilon_e}}$
700	.909	$Z_{0,700} = \frac{132.89\Omega}{\sqrt{\epsilon_e}}$
800	.923	$Z_{0,800} = \frac{138.10\Omega}{\sqrt{\epsilon_e}}$
900	.934	$Z_{0,900} = \frac{142.88\Omega}{\sqrt{\epsilon_e}}$
1000	.943	$Z_{0,1000} = \frac{147.52\Omega}{\sqrt{\epsilon_e}}$

To obtain the impedance values for the sample used, it is necessary to include the dielectric constant for Si ($3.2 \leq \epsilon_r \leq 4.7$). The results for the Si can be seen in table 4.4

For the characteristic impedance for the gap width of 200 nm, it is necessary to use formula 4.10. Using this results in a characteristic impedance of $Z_{0,200} = 55.3\Omega$ for $\epsilon_r = 4.7$, $Z_{0,200} = 64.4\Omega$ for $\epsilon_r = 3.2$ and a mean characteristic impedance of $Z_{0,200} = 59.9\Omega$.

Circular Waveguide

Finally the impedance for the tip has to be calculated. To do this the formulas for circular waveguides are utilised [87]. The circular waveguide consists of a cylindrical tube filled with a dielectric medium. Obviously it is not the exact description for the tip, but should give a good estimate of the impedance. A

Table 4.4: Impedance value for coplanar waveguides on a Si substrate.

size of gap in nm	Impedance for $\epsilon_r = 3.2$ (in Ω)	Impedance for $\epsilon_r = 4.7$ (in Ω)	Mean of Impedance (in Ω)
250	68.4	58.7	63.6
300	72.0	61.8	66.9
400	78.0	66.9	72.5
500	83.2	71.4	77.3
600	87.8	75.3	81.6
700	91.7	78.7	85.2
800	95.3	81.8	88.6
900	98.6	84.7	91.7
1000	101.8	87.3	94.6

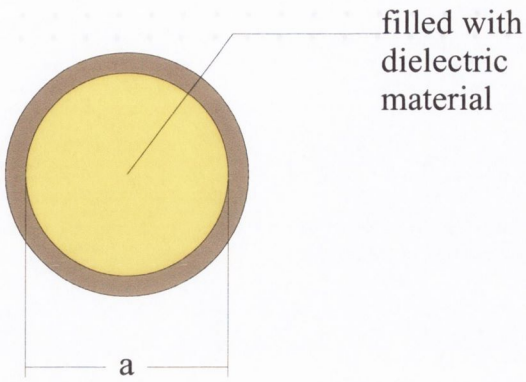

Figure 4.8: This sketch shows a cross-section of a circular waveguide.

sketch of the cross-section can be seen in figure 4.8.

The circular waveguide is cut-off limited and the dimensions used are in the cut-off region already. The cut-off frequency for a circular waveguide is:

$$\lambda_{mn} = \frac{2 \cdot \pi \cdot a}{S_{mn}} \tag{4.11}$$

with $S_{11} = 1.841$ being a Bessel function. The characteristic Impedance for the circular Waveguide is

$$Z_g = \eta \frac{\lambda_g}{\lambda} \tag{4.12}$$

with $\eta = \sqrt{\frac{\mu}{\epsilon}}$ being the intrinsic impedance. μ and ϵ refer to the dielectric medium.

$$\frac{1}{\lambda_g^2} = \frac{1}{\lambda^2} - \frac{1}{\lambda_{mn}^2} \tag{4.13}$$

$$\beta_{mn} = 2 \cdot \pi \cdot \sqrt{\frac{1}{\lambda^2} - \frac{1}{\lambda_{mn}^2}} \tag{4.14}$$

For frequencies below f_{mn}, β becomes imaginary $\Rightarrow \alpha = |\beta|$.

Table 4.5: The cut-off wavelength for different aperture sizes.

Aperture diameter in nm	cut-off frequency λ_{11} in nm
50	85.3
100	170.6
150	256.0

For air the intrinsic impedance is $\eta = 376.7\Omega$ [88].

Combining equation 4.12 and 4.13 we get:

$$\begin{aligned} Z_g &= \eta \cdot \tfrac{1}{\lambda} \cdot \frac{1}{\sqrt{\frac{1}{\lambda^2} - \frac{1}{\lambda_{mn}^2}}} \\ &= \eta \cdot \frac{1}{\sqrt{\frac{\lambda^2}{\lambda^2} - \frac{\lambda^2}{\lambda_{mn}^2}}} \\ &= \eta \frac{1}{\sqrt{1 - \frac{\lambda^2}{\lambda_{mn}^2}}} \end{aligned} \tag{4.15}$$

and replacing equation 4.11 in equation 4.15 results in:

$$Z_g = \eta \cdot \frac{1}{\sqrt{1 - \frac{\lambda^2 \cdot S_{mn}^2}{4 \cdot \pi^2 \cdot a^2}}} \tag{4.16}$$

with a being the value of the radius.

The value for the cut-off frequency has to be determined. It depends on which mode is the dominant one. We use $S_{11} = 1.841$. We then obtain values for λ_{11} with a radius of 50 nm, 100 nm and 150 nm shown in table 4.2.3. Using these results in equation 4.15 yields the following equations, only dependent on the dielectric constant, shown in table 4.2.3

In the formulas of table 4.2.3, η is dependent on the dielectric media inside the Circular waveguide. For air it is $\eta = 376.7\ \Omega$. For glass with a dielectric constant in between $\epsilon_r = 2 - 10$ it becomes:

Table 4.6: Impedance values for different aperture sizes.

Aperture diameter in nm	formula for Z_g
50	$\eta \cdot .136$
100	$\eta \cdot .279$
150	$\eta \cdot .441$

Table 4.7: Impedance value for circular waveguides filled with glass.

Aperture size in nm	Impedance for $\epsilon = 10$ in Ω	Impedance for $\epsilon = 2$ in Ω	Impedance for $\epsilon = 4$ in Ω
50	16.2	36.3	25.6
100	33.3	74.4	52.6
150	52.6	117.6	83.1

$$\eta = \sqrt{\frac{\mu}{\epsilon}} = \sqrt{\frac{\mu}{\epsilon_r \cdot \epsilon_0}} = \frac{120\pi}{\sqrt{\epsilon_r}}$$

which gives a value for η

$$\Rightarrow 119.2\Omega < \eta < 266.6\Omega$$

The impedance for the coated optical fiber is shown in table 4.7. Values given are for the two "extreme" values of glass and also for the value closest to the optical fibre.

42.4 Results on sample with changing gap width

The sample with varying gap between the lines was imaged with the two different polarisations, TM and TE. The scans taken can be seen in figure 4.9a-c

and a cross-section of the marked area in figure 4.9d-f. A clear difference can be seen between the two SNOM images corresponding to TM and TE polarisations. The effect is consistent with the one seen on the samples with the same gap width throughout the whole array (figure 4.5). When imaging the sample with TM polarised light the lines are imaged bright and the gaps are imaged dark. Imaging the same area with TE polarised light shows the opposite contrast, dark lines and bright gaps.

Additionally to the contrast reversal effect, the scan taken with TE polarised light shows a change of intensity in the gap. This can be seen in scan 4.9c and the graph 4.9f. The intensity measured in the gap changes depending on the gap width. It shows an increase in intensity from the 200 nm gap to the maximum intensity at the 400 nm gap and then decreases again. This indicates that the amount of light from the tip is higher at the 400nm gap size compared to the other gap sizes imaged.

Having a closer look at impedance matching shows that if the mismatch would be the smallest for 400 nm this could favour the power output out of the circular waveguide. Increasing the mismatch (increasing or decreasing the gap width) would decrease the power output. Therefore more light would be available when imaging the 400 nm gap compared to the larger and smaller gap sizes and could therefore result in a higher intensity detected in this gap compared to the other gaps.

To get an indication if this model could explain the results it is necessary to use the impedance values calculated in section 4.2.3. The tip used had an estimated aperture of approximately 150 nm. We have arrived to this value by using the shear-force results as well as the measured coating thickness.

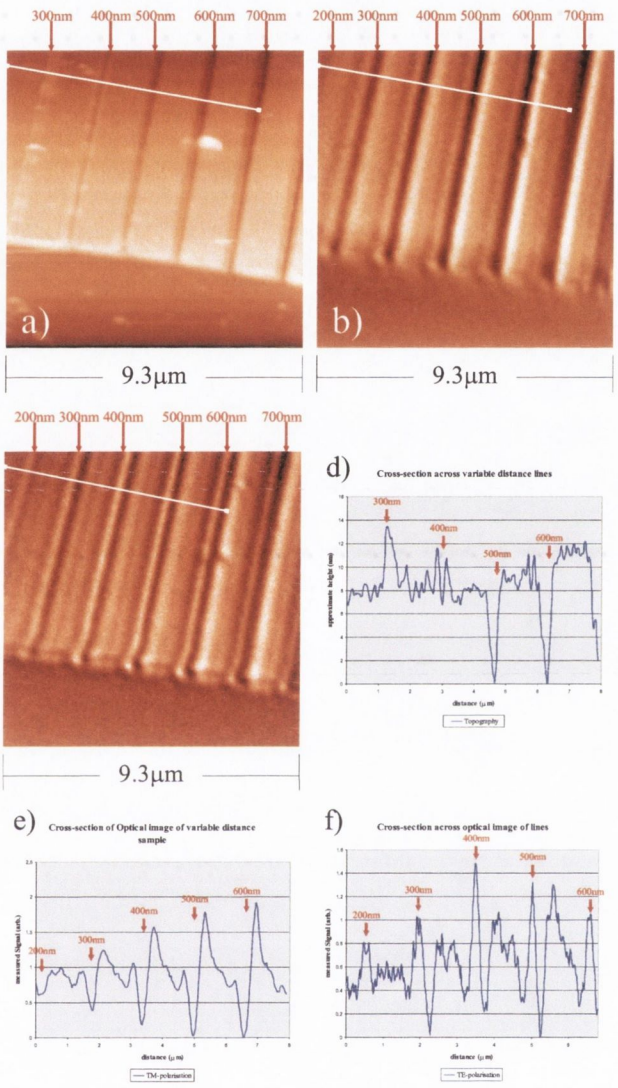

Figure 4.9: This figure shows three scans of the same area. Scan a is a shear-force topography scan. Scans b and c are SNOM images recorded with TM- and TE-polarisation respectively. A contrast reversal between the two optical images can be seen. Additionally, a change of intensity depending on the gap width can be seen in the image taken with TE-polarised light. The highest intensity is visible in the gap with 400 nm. Graphs d-f show cross-sections indicated at scans a-c.

Using this size and comparing it with the calculated impedance value for circular waveguides shows an approximate impedance of 83 Ω. This has to be compared to the values calculated for the coplanar transmission line with a gap width of 400 nm. The result for the coplanar stripline with a gap width of 400 nm is approximately 120 Ω, when using the model for coplanar waveguides the impedance is approximately 73 Ω.

The impedance value for the optical fibre tip is in between the two values calculated for the coplanar stripline and coplanar waveguide, giving a strong indication that the dimension of the structure plays an important role in the effect. This was expected as mentioned in section 4.2.3. It is also closer to the waveguide. This can be understood by the large amount of lines left and right of the gap.

Due to the fact that the maximum value measured in this case was very close to the value of $\frac{\lambda}{2}$, the concern was that the effect could have something to do with this value (resonance effect) rather than impedance matching. Therefore, it was necessary to obtain a similar effect with a different tip with a larger or a smaller aperture diameter. The predicted results for this would be the following. If the aperture diameter decreases, the maximum should shift from the 400 nm gap width to a smaller one. An increased aperture diameter on the other hand would result in a move to a larger gap size.

A second scan taken with a tip having a larger aperture can be seen in figure 4.10a/b and a cross-section of this scan in figure 4.10c/d. It can be seen that the maximum in this scan has moved to a higher value, 600 nm. This was expected due to the larger aperture size. Using the theoretical values of the impedance calculations again shows the following. The transmission

lines with a gap of 600 nm are represented by a characteristic impedance of 134 Ω when using coplanar stripline or 82 Ω when using coplanar waveguide. Taking these values and comparing them to the characteristic impedance of circular waveguides would result in an aperture size of 192 nm. Due to the fact that the tip had a slight tip-crash before the image was obtained, but was prepared in the same fashion as the tip before, the value is realistic.

The move of the maximum from 400 nm to 600 nm when using a different tip for imaging the sample is a strong indication that the polarisation effect observed is related to an impedance matching problem as the most likely explanation.

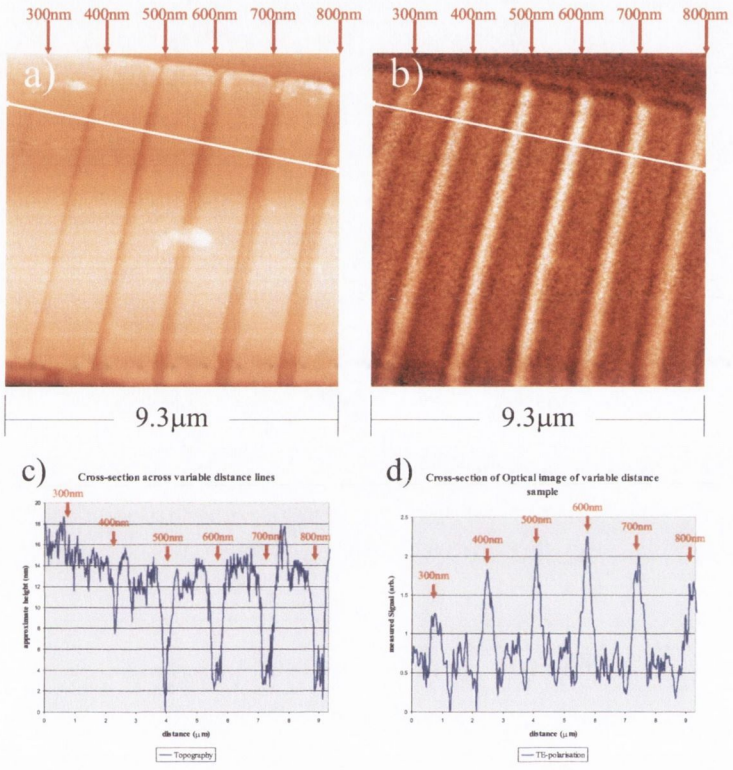

Figure 4.10: Images a and b show scans from the same area as before with a broader tip. Image a shows the topography and Image b shows the SNOM image recorded using TE-polarised light. A similar behaviour as in figure 4.9 can be seen. The only difference is the shift of the maximum to the 600 nm gap. Graphs c and d show cross-sections taken at the lines indicated in scans a and b.

Chapter 5

Conclusions

Two instruments were modified during this study: the reflection-mode SNOM and the fibre pulling machine.

A new shear-force feedback mechanism based on a tuning-fork technique was implemented into the existing SNOM set-up. The advantage of this shear-force system compared to the previous one is that no additional light is needed close to the aperture region.It was tested and calibrated by using calibration samples. Resolutions down to $\sim$ 30 nm (depending on the tip) could be achieved in the shear-force mode for topographic features.

The production of fibre probes for the SNOM and shear-force system was also investigated. A computer controlled fibre pulling machine was fitted with a new pulling mechanism for better reproducibility. Fibre tips with an apex of approximately 100 nm could be produced.

In addition to this, etching techniques were also investigated. The method used to produce fibre tips was the tube etching method. This technique was used at the end of this study. The tip apex had a similar size to the best pulled fibres, but batch processing was possible.

The optical circuit was then tested with different samples and showed resolutions better than $\sim$ 60 nm. Artifacts in the shear-force and the optical part were encountered and analysed

Polarisation SNOM experiments were performed, first the system was tested by using a known sample, an array of transmission lines with a fixed gap width. A contrast reversal between the images taken with TM- or TE-polarised light could be observed. The sample with different gap width in between the lines showed the same contrast reversal. Additionally it showed an intensity change inside the gap depending on the gap width when imaging it with TE-polarised light.

The contrast reversal effect was explained by a favoured output of light for TE-polarisation, while more light is reflected back into the fibre for TM-polarisation. The change of intensity was explained with a dependence of the imaged structure, with impedance matching as one possible candidate. Approximate values for the impedance were achieved with standard microwave formulae. The calculated values showed a matching behaviour and therefore give an indication that this is a suitable explanation for the polarisation effect.

Regarding future work, to further strengthen the point of impedance matching in the optical regime the following experiments could be performed.

(1) Using different types of sample substrates. A shift of the maximum to a different gap width should be observed when imaging the sample with the same tip.

(2) Using different structures with diverging lines could make detection of the position of the maximum easier.

(3) Using a different coloured laser, e.g. Ar-Ion laser. When using the same tip with this laser the maximum should stay at the same position.

(4) Theoretical calculations using finite element method would give a better indication of the exact impedance values.

Additionally to this an electromagnet can be used for imaging magnetic materials in a magnetic field, when the magnetic parts in the legs of the tuning fork are replaced against non-magnetic ones. It would then be possible to do some MOKE experiments, e.g. study hysteresis loops in the near-field regime or magnetic imaging by modulating the magnetic field.

Appendix A

Images of the SNOM/Shear-Force Set-up

Photograph showing the SNOM/shear-force set-up. A side-view of the SNOM / shear-force head can be seen in figure A.1. Anoverview of the SNOM set-up is shown in figure A.2. A view inside the elliptical mirror showing the tip/sample area is shown in figure A.3.

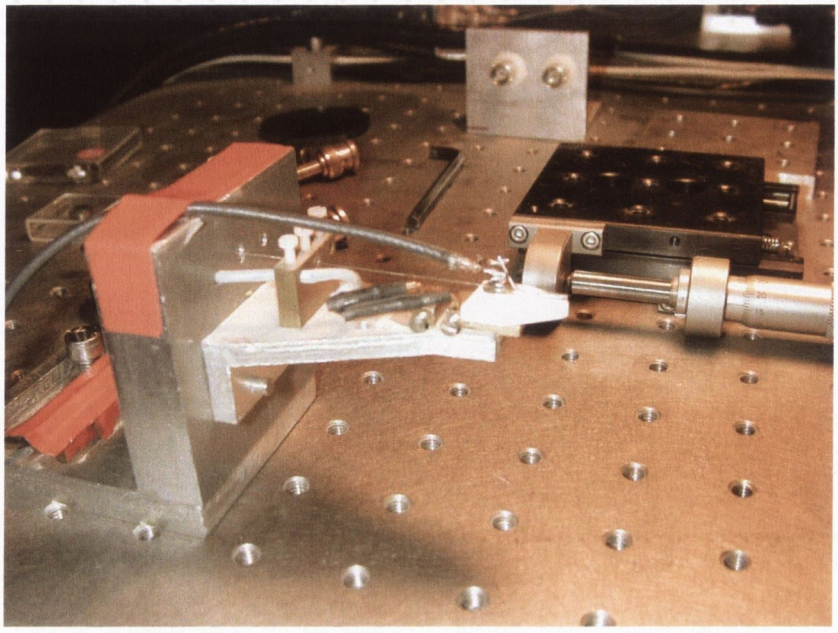

Figure A.1: Sideview of SNOM/shear-force head

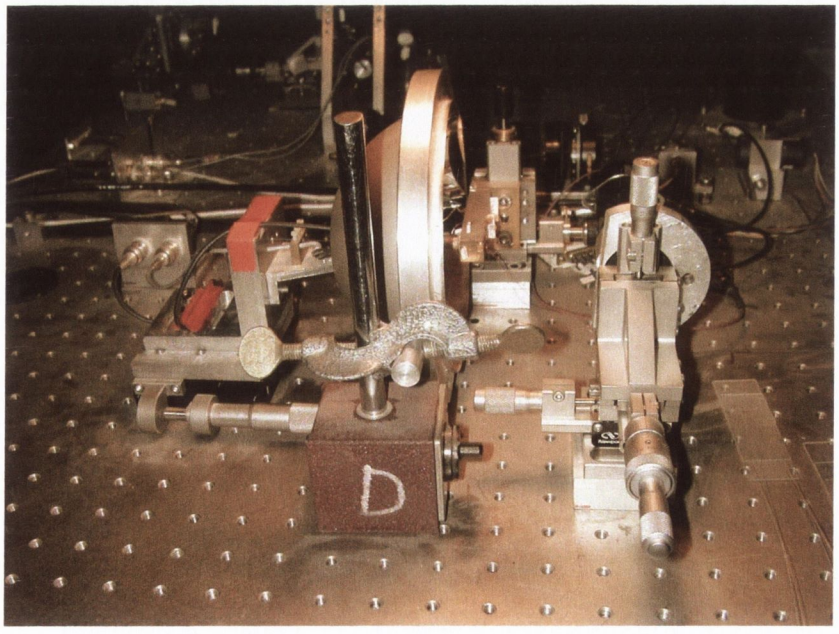

Figure A.2: Overview of SNOM set-up.

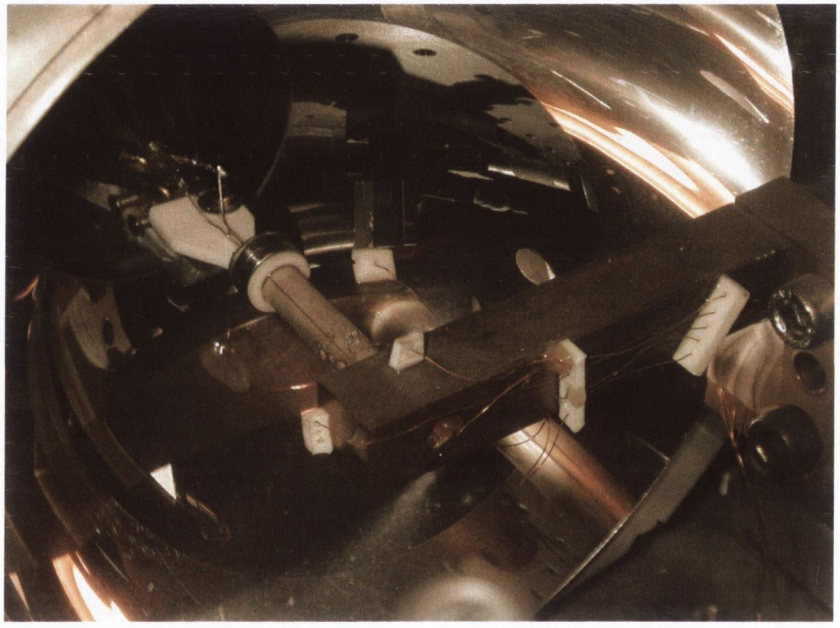

Figure A.3: View into elliptical mirror.

Appendix B

Images of the Pulling machine

Photographs showing the redesigned fibre pulling machine. An overview of the instrument can be seen in figure B.1. A close-up of the pulling mechanism can be seen in figure B.2. For a more detailed description refer to chapter 2

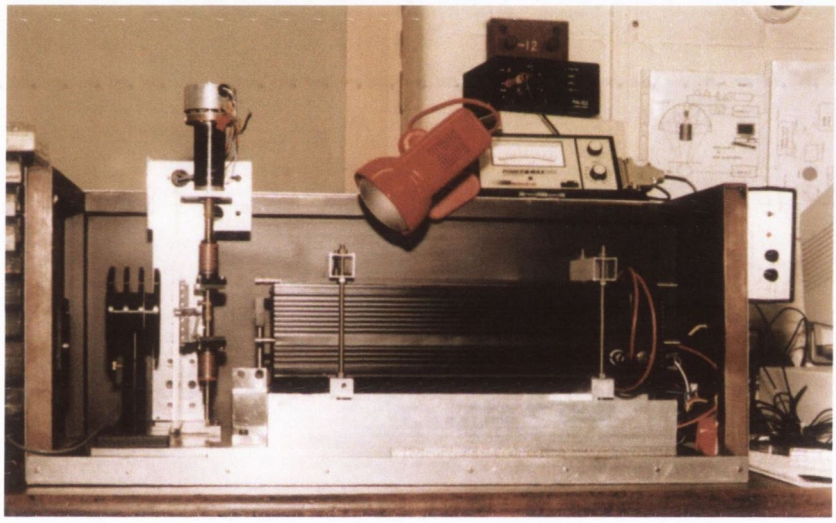

Figure B.1: Overview of the fibre pulling machine.

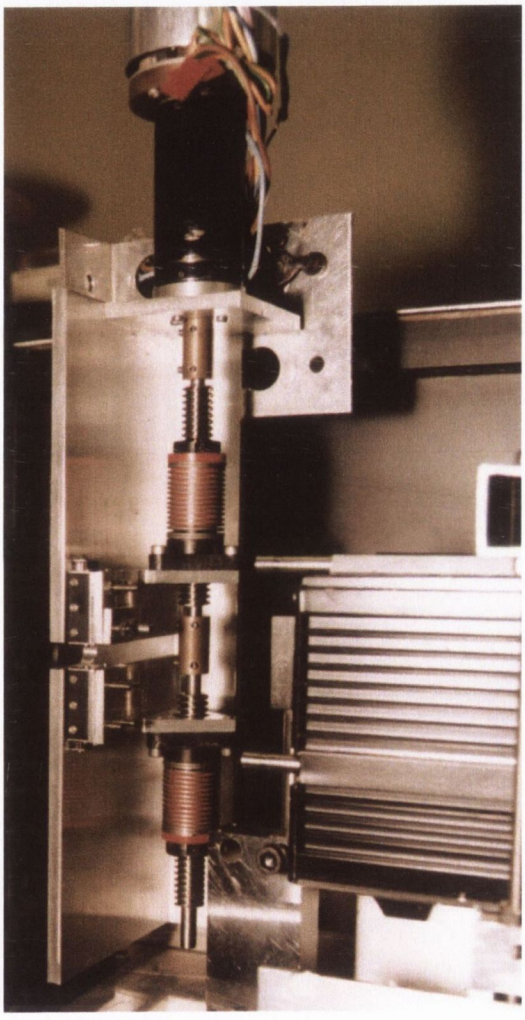

Figure B.2: Close-up of the pulling mechanism.

Bibliography

[1] E. Abbe. *Archiv. f. Mikroskop.*, 9:413, 1873.

[2] M. Born and E. Wolf. *Principles of Optics.* Pergamon Press, 1980.

[3] E. Hecht and A. Zajac. *Optics.* Addison-Wesley Publishing Company, 1974.

[4] G. Mie. *Ann. d. Phys.*, 25:377, 1908.

[5] A. Sommerfeld. *Math. Ann.*, 47:317, 1896.

[6] Lord Rayleigh. *Phil. Mag.*, 43:259, 1897.

[7] C.J. Bouwkamp. PhD thesis, Groningen, 1941.

[8] J.M. Vigoureux and D. Courjon. *Appl. Opt.*, 31(16):3170–3177, Jun. 1992.

[9] D. Courjon, C. Bainier, C. Girard, and J.M. Vigoreux. *Ann. Physik*, 2:149–158, 1993.

[10] Townsend. *A Modern Approach to Quantum Mechanics.* McGraw-Hill International Editions, 1992.

[11] E. Wolf and M. Nieto-Vesperinas. *J. Opt. Soc. Am. A*, 2(6):886–890, Jun. 1985.

[12] Jackson J.D. *Classical Electrodynamics.* Wiley, 1975.

[13] T.L. Ferrell, T.A. Callcott, and R.J. Warmack. *American Scientist*, 73:344–353, 1985.

[14] E.H. Synge. *Phil. Mag.*, 6:356–362, 1928.

[15] E.H. Synge. *Phil. Mag.*, 13(83):297–300, Feb. 1932.

[16] H.A. Bethe. *Phys. Rev.*, 66(7/8):163–182, Oct. 1944.

[17] C.J. Bouwkamp. *Philips Res. Rep.*, 5(5):321–332, 1950.

[18] C.J. Bouwkamp. *Philips Res. Rep.*, 5(6):401–422, 1950.

[19] J.A. O'Keefe. *J. Opt. Soc. Am.*, 46(5):359, May 1956.

[20] A.V. Baez. *J. Opt. Soc. Am.*, 46(10):901, Oct. 1956.

[21] E.A. Ash and G. Nichols. *Nature*, 237:510–516, 1972.

[22] G. Binnig, H. Rohrer, C. Gerber, and E. Weibel. *Phys. Rev. Lett.*, 49(1):57–61, Jul. 1982.

[23] D.W. Pohl, W. Denk, and M. Lanz. *Appl. Phys. Lett.*, 44(7):651–653, Apr. 1984.

[24] A. Lewis, M. Isaacson, A. Harootunian, and A. Murray. *Ultramicroscopy*, 13:227, 1984.

[25] E. Betzig, J.K. Trautman, T.D. Harris, J.S. Weiner, and R.L. Kostelak. *Science*, 251:1468–1470, Mar. 1991.

[26] E. Betzig and J.K. Trautman. *Science*, 257:189–195, Jul. 1992.

[27] E. Betzig. In D.W. Pohl and D. Courjon, editors, *Near Field Optics*, volume E242 of *NATO ASI Series*, pages 7–15. Kluwer Academic Publishers, October 1992.

[28] P. Lorrain, D.P. Corson, and F. Lorrain. *Electromagnetic Fields and Waves.* Freeman, 1988.

[29] L. Novotny and C. Hafner. *Phys. Rev. E*, 50(5):4094–4106, Nov. 1994.

[30] NT-MDT website. http://www.ntmdt.ru/products/snom/.

[31] L. Novotny and D.W. Pohl. In *Photons and Local Probes.*

[32] F. Zenhausern, M.P. O'Boyle, and H.K. Wickramasinghe. *Appl. Phys. Lett.*, 65(13):1623–1625, September 1994.

[33] F. Zenhausern, Y. Martin, and H.K. Wickramasinghe. *Science*, 269(5227):1083–1085, August 1995.

[34] D. Courjon and C. Bainier. *Rep. Prog. Phys.*, 57:989–1028, 1994.

[35] E. Betzig. In D.W. Pohl and D. Courjon, editors, *Near-Field Optics*, pages 7–15, 1993.

[36] D.W. Pohl. *Advances in Optical and Electron Microscopy.* 1991.

[37] M.A. Paesler and P.J. Moyer. *Near-Field Optics.* Wiley-Interscience, 1996.

[38] T.J. Silva and S. Schultz. In D. Courjon D. W. Pohl, editor, *Near Field Optics*, volume E242 of *NATO ASI Series*, pages 263–272. Kluwer Academic Publishers, October 1992.

[39] T.J. Silva, S. Schultz, and D. Weller. *Appl. Phys. Lett.*, 65(6):658–660, August 1994.

[40] D.W. Pohl, W. Denk, and U. Duerig. In *Micron and Submicron Integrated Circuit Metrology*, volume 565 of *SPIE*, pages 56–61, 1985.

[41] U. Dürig, D.W. Pohl, and F. Rohner. *J. Appl. Phys.*, 59(10):3318–3327, May 1986.

[42] E. Betzig, M. Isaacson, H. Barshatzky, A. Lewis, and K. Lin. In *Scanning Microscopy Technologies and Applications*, volume 897 of *SPIE*, pages 91–99, 1988.

[43] M.A. Paesler and P.J. Moyer. *Near-Field Optics*, chapter 2.3.2, page 27. Wiley-Interscience, 1996.

[44] U.Ch. Fischer, U.T. Dürig, and D.W. Pohl. *Appl. Phys. Lett.*, 52(4):249–251, Jan. 1988.

[45] R.D. Grober, T.D. Harris, J.K. Trautman, and E. Betzig. *Rev. Sci. Instrum.*, 65(3):626–631, Mar. 1994.

[46] R.D. Grober, T.D. Harris, J.K. Trautman, E. Betzig, W. Wegscheider, L. Pfeiffer, and K. West. *Appl. Phys. Lett.*, 64(11):1421–1423, Mar. 1994.

[47] I. Hörsch, R. Kusche, O. Hollricher, O. Kirschenhofer, O. Marti, R. Sieber, G. Krausch, and J. Mlynek. In R. Möller O. Marti, edi-

tor, *Photons and Local Probes*, volume E300 of *NATO ASI Series*, pages 139–144. Kluwer Academic Publishers, September 1994.

[48] H. Bielefeldt, I. Hörsch, G. Krausch, J. Mlynek, and O. Marti. *Appl. Phy. A*, 59(2):103–108, Aug. 1994.

[49] C. Durkan and I.V. Shvets. *Ultramicroscopy*, 61:227–231, 1995.

[50] R.C. Reddick, R.J. Warmack, and T.L. Ferrell. *Phys. Rev. B*, 39(1):767–770, Jan. 1989.

[51] G. Binnig, C.F. Quate, and Ch. Gerber. *Phys. Rev. Lett.*, 56(9):930–933, 1986.

[52] P.C. Yang, Y. Chen, and M. Vaez-Iravani. *J. Appl. Phys.*, 71(6):2499–2502, Mar. 1992.

[53] E. Betzig, P.L. Finn, and J.S. Weiner. *Appl. Phys. Lett.*, 60(20):2484–2486, May 1992.

[54] R. Toledo-Crow, P.C. Yang, Y. Chen, and M. Vaez-Iravani. *Appl. Phys. Lett.*, 60(24):2957–2959, Jun. 1992.

[55] J.J. Greffet and R. Carminati. *Progress in Surf. Sci.*, 56(3):133–237, 1997.

[56] D. van Labeke and D. Barchiesi. In D. W. Pohl and D. Courjon, editors, *Near Field Optics*, volume E242 of *Series E: Applied Sciences*, pages 157–178. Kluwer Academic Publishers, 1993.

[57] Ch. Girard and M. Spajer. *Appl. Opt.*, 29(26):3726–3733, Sep. 1990.

[58] D. Barichiesi and D. van Labeke. In D.W. Pohl and D. Courjon, editors, *Near Field Optics*, volume 242 of *Series E: Applied Sciences*, pages 179–188, 1992.

[59] J.J. Greffet and F.R. Ladan. *J. Opt. Soc. Am. A*, 8(8):1261–1269, Aug. 1991.

[60] C. Girard. *Phys. Rev. B*, 45(4):1800–1810, Jan. 1992.

[61] J. Cites, M.F.M. Sanghadasa, C.C. Sung, R.C. Reddick, R.J. Warmack, and Ferrell T.L. *J. Appl. Phys.*, 71(1):7–10, Jan. 1992.

[62] Colm Durkan. *Reflection-Mode Scanning Near-Field Optical Microscopy (SNOM).* PhD thesis, University of Dublin, Trinity College, May 1996.

[63] Y. Kuk and P.J. Silverman. *Rev. Sci. Instrum.*, 60(2):165–178, 1989.

[64] Newport, http://www.newport.com. *Newport Catalogue.*

[65] C.J. Chen. *Introduction to Scanning Tunneling Microscopy.* Oxford University Press, 1993.

[66] Staveley Sensors Inc. *EBL Product Line.*

[67] Melles Griot. *Melles Griot Catalogue.*

[68] Hamamatsu. *Photo Multiplier Tubes.*

[69] Hamamatsu. *Datasheet for R928 PMT.*

[70] Laser 2000. *Laser 2000 Catalogue.*

[71] E. Betzig, M. Isaacson, and A. Lewis. *Appl Phys. Lett.*, 51(25):2088–2090, Dec. 1987.

[72] Sutter Instrument Company. *P-2000 Laser based Micropipette/fiber puller datasheet.*

[73] R. Stockle, C. Fokas, V. Deckert, R. Zenobi, B. Sick, B. Hecht, and U.P. Wild. *Appl. Phys. Lett.*, 75(2):160–162, Jul 1999.

[74] P. Hoffmann, B. Dutoit, and R.P. Salathe. *Ultramicroscopy*, 61(1-4):165–170, Dec 1995.

[75] D. Courjon, C. Bainier, and M. Spajer. *J. Vac. Sci. Technol. B*, 10(6):2436–2439, Nov./Dec. 1992.

[76] C. Durkan and I.V. Shvets. *Appl. Phys. Lett.*, 79(3):1219–1221, Feb. 1996.

[77] C. Durkan and I.V. Shvets. *J. Appl. Phys.*, 80(10):5659–5664, Nov. 1996.

[78] C. Durkan and I.V. Shvets. *Appl. Opt.*, 36(31):8173–8178, Nov. 1997.

[79] K. Karrai and R.D. Grober. *Appl. Phys. Lett.*, 66(14):1842–1844, Apr. 1995.

[80] J. Baretz, O. Hollricher, and O. Marti. *Rev. Sci. Instrum.*, 67(5):1912–1916, May 1996.

[81] R. Brunner, A. Bietsch, O. Hollricher, and O. Marti. *Rev. Sci. Instrum.*, 68(4):1769–1772, Apr. 1997.

[82] R. Kantor, M. Lesnak, N. Berdunov, and I.V. Shvets. *Appl. Surf. Sci.*, 144-145:510–513, 1999.

[83] Roman Kantor. *Scanning Near-Field Microscopy of Microwave Circuits.* PhD thesis, University of Dublin, Trinity College, 2001.

[84] *Sample provided by Mikroelektronik Centret, DTH, 2800 Lyngby, Danmark.*

[85] E. Jurdik, J. Hohlfeld, H. van Kempen, T. Rasing, and J.J. McClelland. *Appl. Phys. Lett.*, 80(23):4443–4445, Jun 2002.

[86] E. Betzig, J.K. Trautman, J.S. Weiner, T.D. Harris, and R. Wolfe. *Appl. Opt.*, 31(22):4563–4568, Aug. 1992.

[87] K.F. Sander. *Microwave Components and Systems.* Electronic Systems engineering series. Addison-Wesley Publishing Company, 1987.

[88] Kraus J.D. *Electromagnetics.* McGraw-Hill, 1992.

Presentation and Publication List

1. Near-Field Optics 7 Conference, Rochester, NY, oral presentation:
A. Gademann, I.V. Shvets and C. Durkan
"Study of the influence of the optical impedance matching onto near-field optical microscopy imaging in polarization mode"

2. A. Gademann, C. Durkan, I.V. Shvets *Journal of Physics D: Applied Physics* (accepted, published in 2003)

3. A. Gademann, C. Durkan, I.V. Shvets *Journal of Applied Physics* (submitted)